



Supplementary Information for

The extent of soil loss across the U.S. Corn Belt

Authors: Evan A. Thaler, Isaac J. Larsen, Qian Yu

Correspondence to: ethaler@geo.umass.edu

This PDF file includes:

Materials and Methods
Figs. S1 to S17
Table S1
Data availability statement
References for SI citations

Materials and Methods

Initial condition of the soil organic carbon index

Our interpretation that the exposure of soils with low soil organic carbon (SOC) concentrations on convex hilltops indicates a SOC-rich A-horizon was eroded relies on the assumption that hilltops in the Corn Belt maintained a layer of SOC-rich soil prior to cultivation. Native prairie remnants record the pre-disturbance soil catena (1), but the permanent vegetation cover in the prairie precludes application of the satellite-derived soil organic carbon index (SOCi) (2) to assess the distribution of SOCi throughout the prairies. Hence, we collected soil cores from hilltops in a native prairie in Iowa to directly measure the SOCi for the prairie soils and then compared the SOCi values to soil samples collected from the surface of hilltops in an adjacent agricultural field (Fig. S1). Each soil sample was dried, sieved to < 2 mm, and the spectral reflectance was measured using an ASD FieldSpec 4 with a Muglight attachment. SOCi for the samples was calculated from the spectral reflectance data following (2).

The three cores collected on convex topography (Fig. S1a-b) in the prairie display high SOCi values at the surface that decline with depth (Fig. S1c-e), consistent with previous measurements of SOC-depth profiles (3). The mean SOCi value for the uppermost 1 cm in the prairie samples is 6.5, and the high SOCi values in near-surface soils is consistent with our assumption that hilltops in native prairies had SOC-rich A-horizon soils prior to cultivation. On the three sampled hilltops in the adjacent agricultural field (Fig. S1f), the mean SOCi value of the ten surface samples is 2.4, which corresponds to SOCi values for the 30-40 cm depth interval of the prairie soils, suggesting an equivalent thickness of soil has been lost from the hilltops.

Topographic analysis

LiDAR topographic data were downloaded from the USGS (4) and from individual state data repositories. To determine the appropriate resolution for measuring topographic curvature (∇^2), we calculated curvature from test digital elevation models (DEM) with resolutions that varied from 2 to 15 m in 1 m increments. For each grid size, curvature values were extracted from a polygon containing a hilltop, hillslope, and hollow, and the interquartile range (IQR) (25th to 75th percentiles) was calculated (Fig. S3). We find that the IQR of curvature decreases with increasing grid size, indicating greater terrain roughness at lower grid sizes. At the 4 m grid size, there is a break in the scaling, such that the IQR of curvature shows relatively little variation with increasing grid size. Following prior work (5), we interpret the scaling break to differentiate between landscape-scale hilltop-hollow topography and smaller-scale topographic roughness generated, by, for example, plowing. Hence we resampled the LiDAR-derived DEMs to a 4 m spatial resolution to capture the landscape-scale hilltop and hollow topography in our analyses. Slope and topographic curvature values were calculated as the first and second derivative of elevation, respectively.

Cumulative distributions of topographic curvature were extracted from all of the analyzed fields within each of the 28 individual study sites (Fig. S15) and for the region-wide dataset by first binning the curvature data into 50 bins of uniform width. The median slope values shown in Fig. 3 were calculated for all the pixels located within each curvature bin.

Image processing

High-resolution satellite images (WorldView-2, WoldView-3, Quickbird-2, and GeoEye-1) provided by the Commercial Archive Data for NASA Investigators (6) or the Polar Geospatial Center were orthorectified using the rational polynomial coefficient orthorectification workflow

in ENVI 5.4. The images were radiometrically corrected using an empirical line correction method (7). A clear water pixel and an aluminum metal roof pixel were identified and calibrated against the known reflectance of distilled water and aluminum metal roofing using data from the ASTER spectral library (8). The SOCI was calculated for each image and the resulting rasters were resampled to a spatial resolution of 4 m to match the resolution of the curvature grids.

Relating laboratory- and satellite-derived SOCI

The Rapid Carbon Assessment (RaCA), undertaken by the Soil Science Division of the USDA National Resource Conservation Service, collected 144,833 soil samples to 1 m depth at 6,148 sites in the conterminous United States (9). The soil horizon each sample was collected from was determined in the field, and the samples were air-dried and hyperspectral reflectance was measured from 350-2500 nm using a laboratory spectroradiometer and SOC was measured on the dry samples (10, 11). We scaled the RaCA-derived SOCI values to the same range as the satellite-derived SOCI values, which are offset from one another due to different measurement conditions, such as atmospheric effects. The re-scaling used the relationship in Figure 5 of Thaler et al. (2), and the methods described therein.

Antecedent precipitation and surface soil moisture

Previous work has demonstrated that the soil surface dries rapidly following precipitation and becomes decoupled from soil moisture at depth (12). Hence we evaluated the timing and magnitude of precipitation prior to image acquisition for each of the 28 sites to qualitatively assess whether the soil surface, which is imaged by the satellites, was likely to have been dry at the time of image acquisition. For each site, precipitation data were downloaded from the nearest

weather station that is part of the Hourly Precipitation Dataset, archived at the National Climatic Data Center. At the 28 sites, the minimum time between image acquisition and previous rainfall was 20 hours, with a mean of 73 hours, and the mean amount of precipitation was 10 mm (Fig. S9). Previous observations have indicated that the soil surface becomes completely dry after three to four days (12), and our own observations throughout the study area suggest a faster drying rate, as even following nightly rainfall, the soil surface is typically dry after a full day of summer sunlight. These results suggest the soil surface would have been dry when the cloud-free images were acquired. The predicted B-horizon exposure at sites where rainfall occurred < 72 hours and > 72 hours before image acquisition are $31 \pm 7\%$ and $30 \pm 7\%$, respectively. Hence the predicted B-horizon exposure is indistinguishable for sites with different rainfall timing which is consistent with a lack of a soil moisture influence on our results.

Effect of moisture on the SOCI

Increases in SOC and soil moisture result in decreased reflectance in the visible spectrum and cause soils to appear darker (13). We assessed the effect of soil moisture on the SOCI for soils with a range of SOC by measuring soil spectral reflectance under dry and saturated moisture levels. The spectra used to calculate the soil organic carbon index values were measured using an ASD FieldSpec 4 with a Muglight attachment. Soil organic carbon was measured using a Costech elemental analyzer (ECS 4010) following removal of inorganic carbon with 1 N HCl. We found that the magnitude of the increase in the SOCI as a function of soil moisture is related to the SOC concentration of the sample. For samples with the largest concentration of SOC ($\sim 4\%$), there is a factor of four increase in the SOCI, whereas the SOCI increases by a maximum of a factor of three for samples with $< 1\%$ SOC (Fig. S10).

The spectral measurements of RaCA soil samples used to develop the logistic regression analysis that informed our classification of A- and B-horizon soils in the satellite images were made on dried soils. We assessed the impact of soil moisture on the classification of soil horizons by adjusting the SOCI values for the RaCA samples according to our experimental results. For A-horizon samples, which have a range of SOC from ~1.0% to 9.0%, the SOCI values were conservatively increased by a minimum factor of three and a maximum factor of four. Similarly, B-horizon samples, which have a range of SOC from ~0.5% to 2.5%, the SOCI values were increased by a minimum factor of two and a maximum factor of three. In our framework, samples with SOCI values less than the value represented by the 50% probability threshold are classified as B-horizon. For each set of RaCA calibration samples for the 28 study sites, we recalculated the classification threshold for five soil moisture cases: 1) the minimum effect of soil moisture on the A-horizon SOCI values and dry B-horizon values, 2) the minimum effect of soil moisture on both the A- and B-horizon SOCI values, 3) the maximum effect of soil moisture on the A-horizon and dry B-horizon SOCI values, 4) the maximum effect of soil moisture on the A-horizon and the minimum effect on the B-horizon SOCI values, and 5) the maximum effect of soil moisture on both the A- and B-horizon SOCI values. We simulated a variety of scenarios because topographic influences on soil moisture may result in different moisture levels throughout a landscape. The thresholds were applied to images for each of the 28 study sites and the fraction of the land area with exposed B-horizon soil was calculated (Fig. S12). Increasing soil moisture increases the A- and B-horizon SOCI values and hence increases the threshold SOCI value, such that samples classified as A-horizon when dry are classified as B-horizon when wet (Fig. S11). When the moisture-adjusted thresholds are applied to the images, the fraction of pixels classified as B-horizon increases relative to the threshold developed using

the SOCI values from dried soil samples. Because the SOCI values in the image are lower than the predicted values for moisture-adjusted sample values, the thresholds calculated using samples adjusted for soil moisture reclassify A-horizon pixels as B-horizon. Hence, our estimate of topsoil loss based on the threshold developed using the dry RaCA samples is a minimum if any moisture is present in the analyzed fields.

Relationship between SOC and the SOCI

The relationship between SOC and the satellite-derived SOCI was validated at five agricultural fields across the U.S. (Fig. S13). Two of the sites are in areas with till-derived soils (Fig S14a, d), and the two other sites are in areas with loess-derived soils (Fig.14b, c) within the Corn Belt region (14-16). At the four sites, the coefficient of determination (R^2) ranges from 0.63 to 0.68. The relationship was also validated at a fifth site ($R^2 = 0.72$), located in Maryland (Fig. S14e) (17), which demonstrates the validity of the index beyond the Corn Belt region. Additionally, the correlation between the SOCI and the SOC was assessed for each set of RaCA soil samples within a 50 km buffer of each of the 28 field sites. The mean R^2 value of the correlations is 0.8 (Fig. S6), indicating that the SOCI predicts SOC very well within the study area.

Relationship between SOCI and topography

The relationship between SOC, SOCI, and topographic curvature was examined at the four SOCI validation sites in the Corn Belt (Fig. S14). Consistent with observations and interpretations at the 28 sites (Fig. 3), low SOC and SOCI values are observed on the most

convex topography (negative curvature), and the SOC and SOCI values increase as curvature increases. At the two sites in the till-derived soils (Fig. S14b, c), where the sampling point density is higher than the other two sites, the full range of values is observed at the transition from concave to convex topography, an observation consistent with both B-horizon exposure via water erosion and deposition of A-horizon from tillage translocation at those locations (16) .

Determination of soil parent material

To determine the spatial distribution of till-and loess-derived soils, we used the United States Geological Survey map of surficial deposits and the inferred ice limit of the last glacial maximum (LGM) compiled from 31 individual quadrangles mapped at a 1:1,000,000 scale (18). We presume that areas north of the LGM are composed of soils derived from glacial till surficial deposits, whereas soils south of the LGM are developed primarily from loess. Loess deposits have been mapped in the Driftless Area, a region that was not glaciated during the LGM (19). Hence, we classify soil in the Driftless Area as loess-derived.

Calculation of economic losses

We calculated economic losses based on data for corn and soybean production, as, on average, these two crops make up 95% (20) of the area planted in each county within the study area. We used results from a comprehensive study of the influence of erosion on corn yields in Iowa to assess declines in productivity. Prior work has shown that in mollisols, complete topsoil loss produces similar decreases in crop yields for corn and soybeans (18), hence we assume the fractional yield losses for soybeans are the same as for corn. We calculate economic losses based

on our estimates of the area with exposed B-horizon soil, and the mean corn and soybean prices, hectares planted, and yields (Fig. S16) from 2012-2018 using data from the U.S Department of Agriculture National Agricultural Statistics Service. Corn yields were previously evaluated at 569 sites in 44 counties in Iowa, where categorical measurements of soil erosion were also evaluated (21). The sites include areas where soil parent materials are glacial till and loess. The erosional severity of soils was classified by the amount of A-horizon remaining, as no erosion to slight severity (>18 cm remaining), moderate severity (8-18 cm remaining), and severe (< 8 cm remaining). In soils developed from glacial till, corn yields decreased 55,800 kg km⁻² as soils became moderately eroded and further decreased 81,500 kg km⁻² when soils became severely eroded. Similarly, corn yields in loess-derived soils decreased by 36,400 kg km⁻² for moderately eroded soils and further decreased by 30,700 kg km⁻² when soils were severely eroded (21). Because topsoil has been completely eroded at the sites for which we calculate economic losses, and thus would be classified as severely eroded, we sum the decreased corn yields from slight to severe, giving estimated reduction of 137,300 kg km⁻² for soils formed from glacial till and 67,100 kg km⁻² for loess-derived soils.

Based on the hectares planted of corn (Fig. S16a) and soybeans (Fig. S16d), predicted areas of topsoil loss (mean loss \pm 1 S.D.), reductions in corn (Fig. S16b) and soybean (Fig. S16e) yields due to complete topsoil loss, and the average corn and soybean prices from 2012-2018 (US\$0.15 kg⁻¹ and \$0.37 kg⁻¹, respectively) (22), we estimate the mean annual economic losses per county for decreased corn (Fig. S16c) and soybeans (Fig. S16f). Annual economic losses were calculated as: Annual losses per county [USD county⁻¹] = Exposed B-horizon area [ha county⁻¹] * mean yield [kg ha⁻¹] * fraction decrease due to A-horizon erosion * crop price [USD

kg⁻¹], where USD is U.S. dollars. We further estimated economic losses at the farm-level (Fig. 4d) by dividing the county-level losses by the number of farms in each county (Fig. S16g) (23).

Data availability

Data are cataloged at the Oak Ridge National Laboratory Distributed Active Archive Center (<https://doi.org/10.3334/ORNLDAAAC/1774>) (24). The archive includes spatial raster data for topographic metrics (elevation, slope, curvature), soil organic carbon index values, and the probability of B-horizon soil. Spatial vector data and tabular data with county-, state-, and farm-level erosion and economic loss values are also archived. The soil organic carbon index values, derived from the RaCA samples, and used to develop the logistic regression and receiver operator characteristic curve for each site (such as those shown in Fig. S8) are also archived.

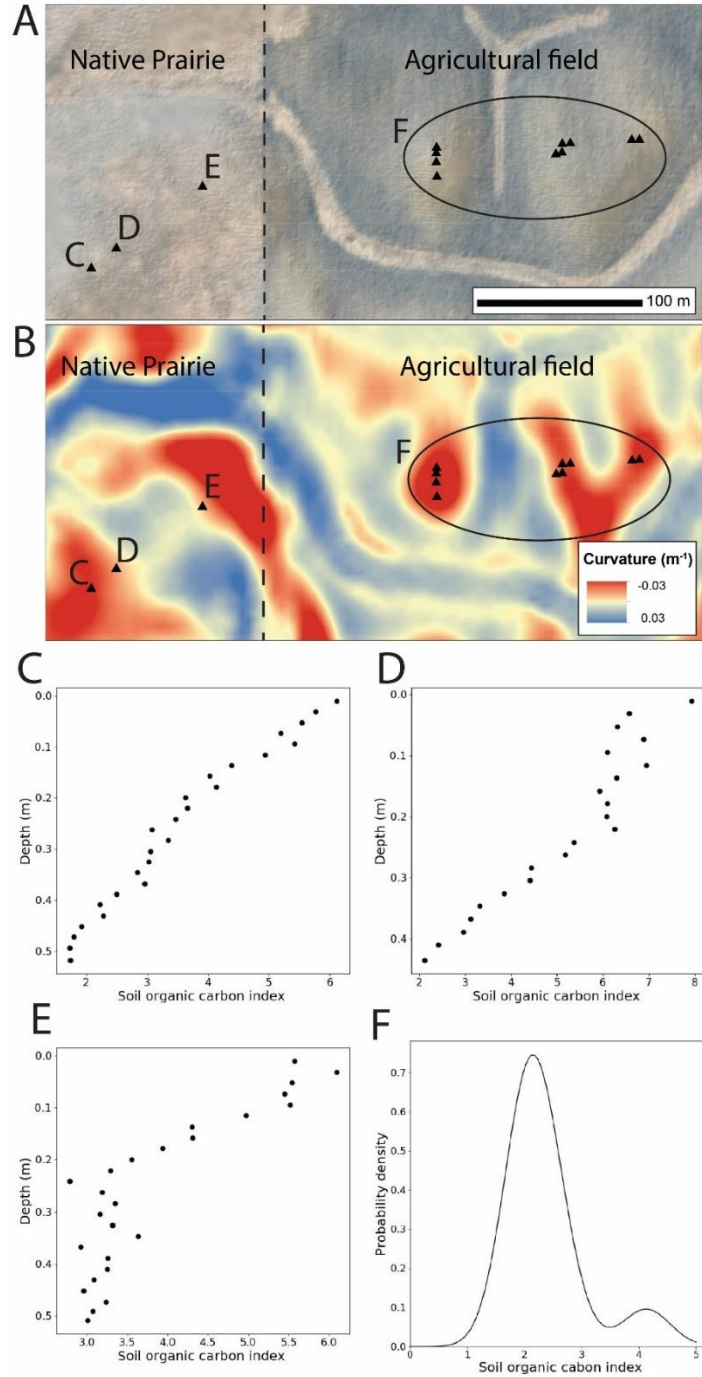


Fig. S1. The Soil Organic Carbon Index (SOCI) values measured for three soil cores from a native prairie in Iowa and surface soil samples from an adjacent agricultural field. A) True-color WorldView-2 image showing location of prairie cores (C, D, E) and surface samples from the field (F) B). Map of topographic curvature where red pixels denote negative curvature (convex topography) and blue pixels denote positive curvature (concave topography). The SOC depth profiles from the prairie cores are shown in panels C-E. F) The distribution of SOC values for surface soil samples collected in the adjacent agricultural field. Locations of the samples are

shown in panels A and B. Image credit: ©2015 DigitalGlobe, Inc., a Maxar company, NextView License.

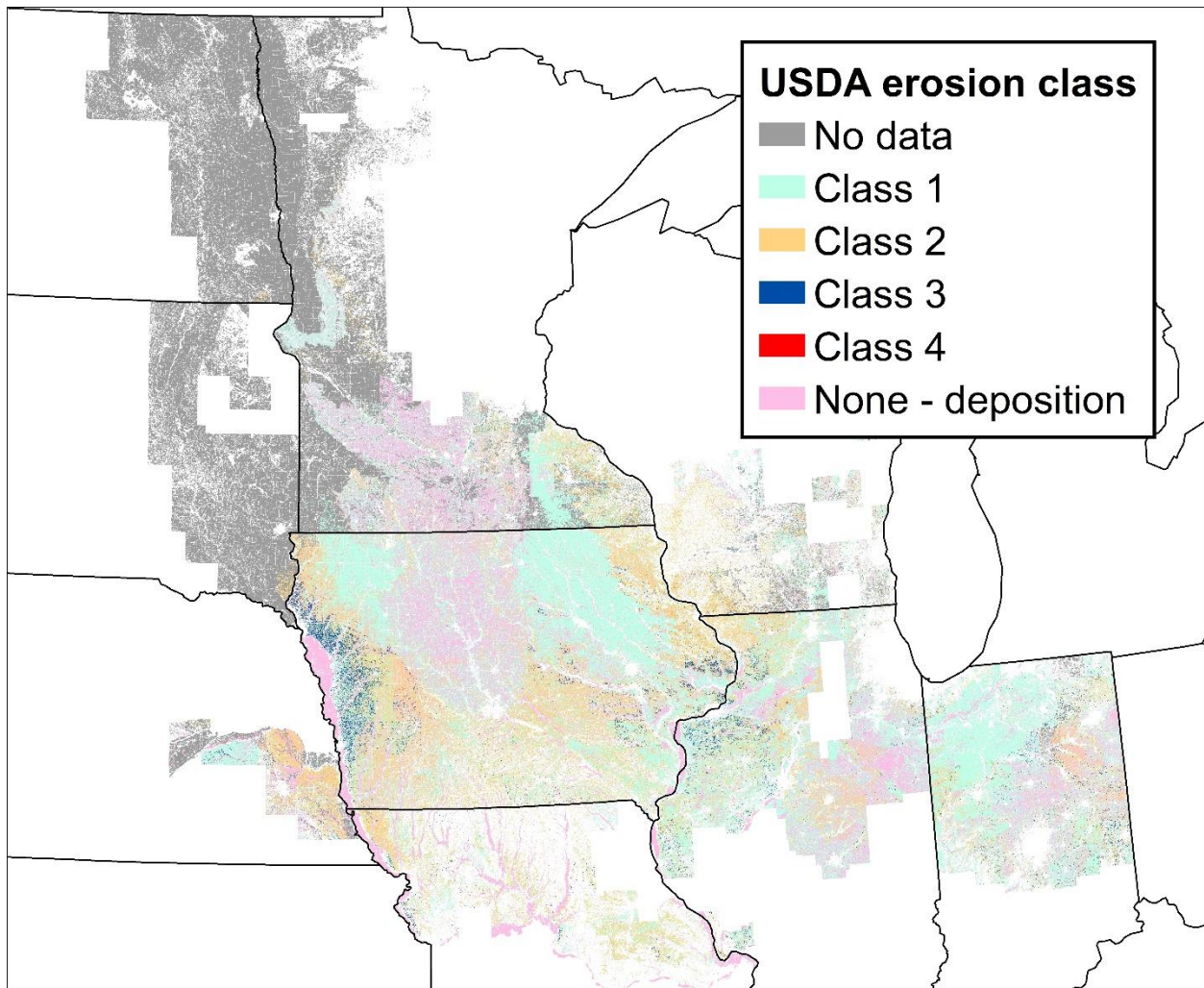


Fig. S2. Map of erosion classes assigned by the U.S. Department of Agriculture (25). 31% of the soils in the area have soils with Class 1 erosion, 16% have Class 2 erosion, 3 % have Class 3 erosion, 0% have Class 4 erosion, 15% of soils are classified as having no erosion or as depositional sites, and classification data are not available for 35% of soils. Class 4 is equivalent to the complete loss of A-horizon measured by our analysis.

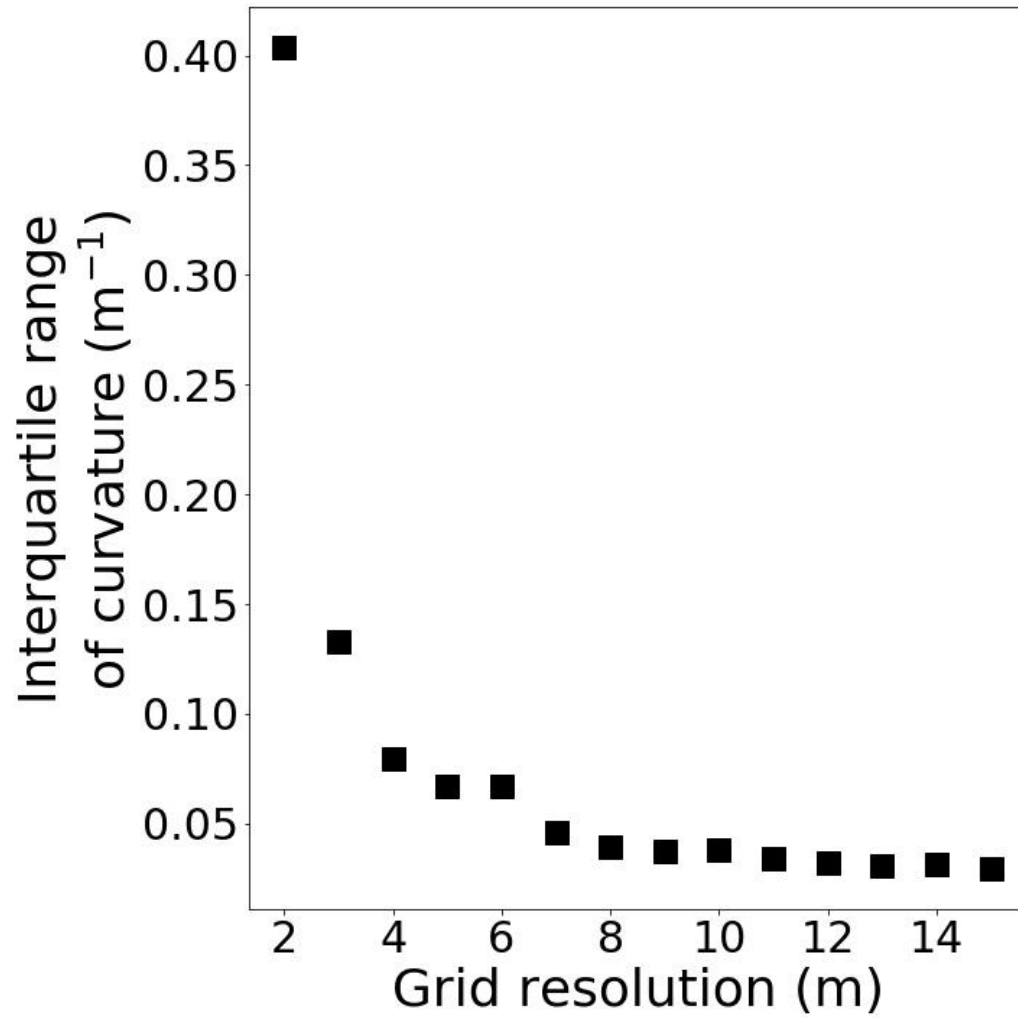


Fig. S3. The interquartile range of curvature values calculated using grid resolutions ranging from 2 m to 15 m.

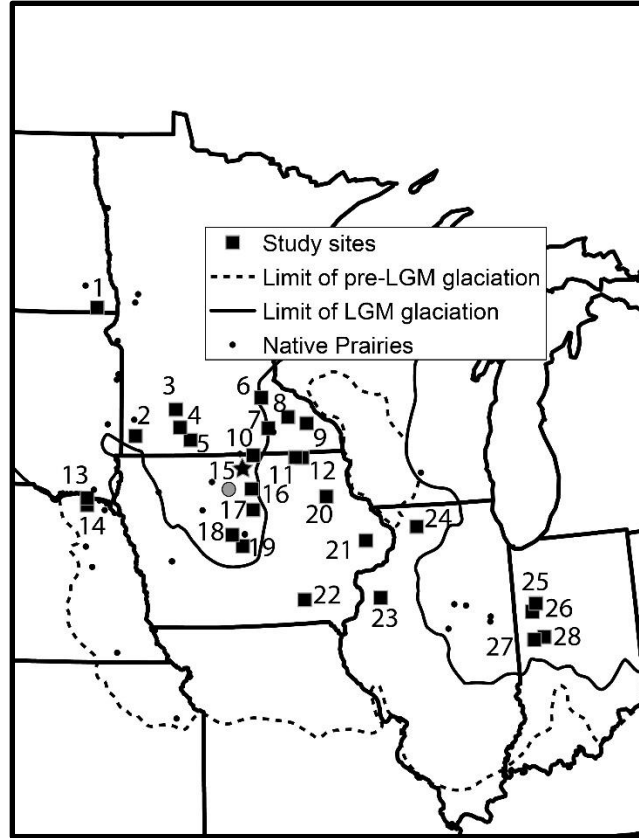


Fig. S4 Location of study sites with numbers corresponding to study sites in Fig. S17 and in the ORNL DAAC data repository. The gray circle shows the location of the native prairie and adjacent agricultural field shown in Fig. S1, and the star indicates the location of the example field shown in Fig. 2. The dots indicate the location of soil samples collected on convex topography in native prairies (26) that were used to estimate the organic carbon stock to 30 cm-depth.

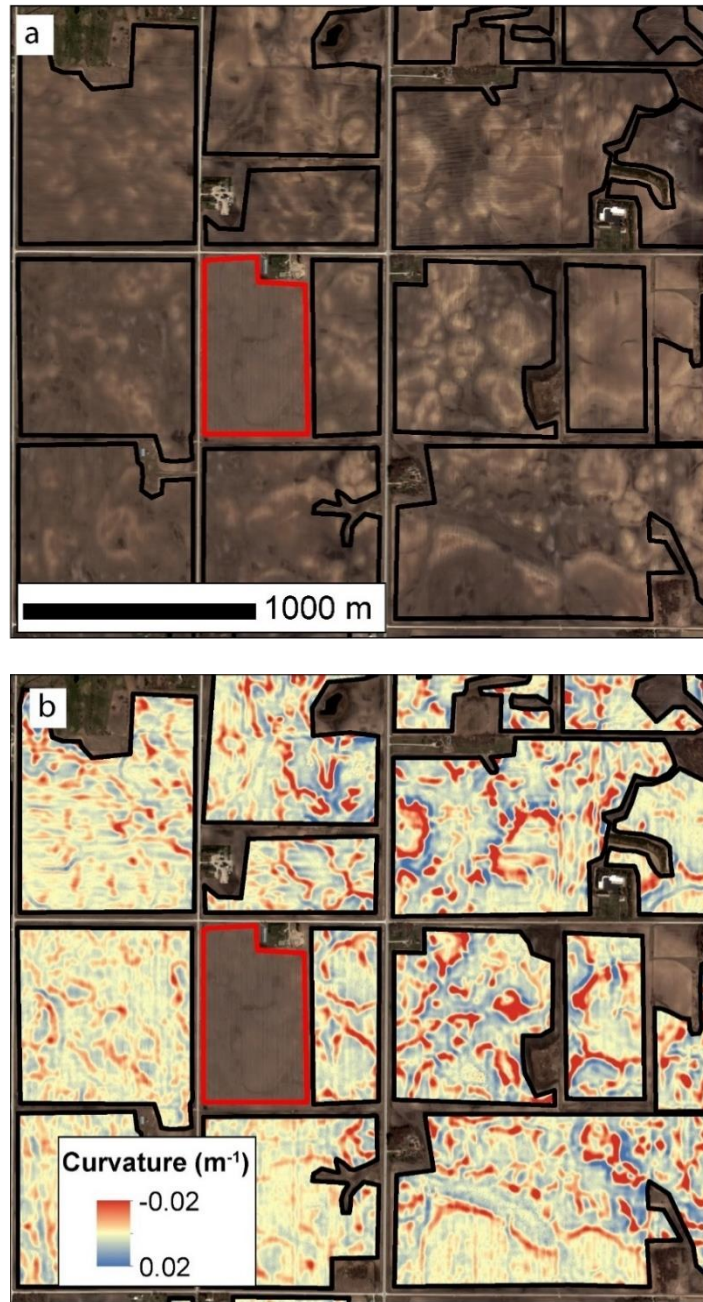


Fig. S5. An example study site comprised of multiple fields shown in (a) true color and (b) topographic curvature. The black polygons surround plowed fields with bare soil. The field within the red polygon contains crop residue and such fields are excluded from the analysis, as are areas such as fence lines and grass waterways where bare soil is not exposed. Image credit: ©2015 DigitalGlobe, Inc., a Maxar company, NextView License.

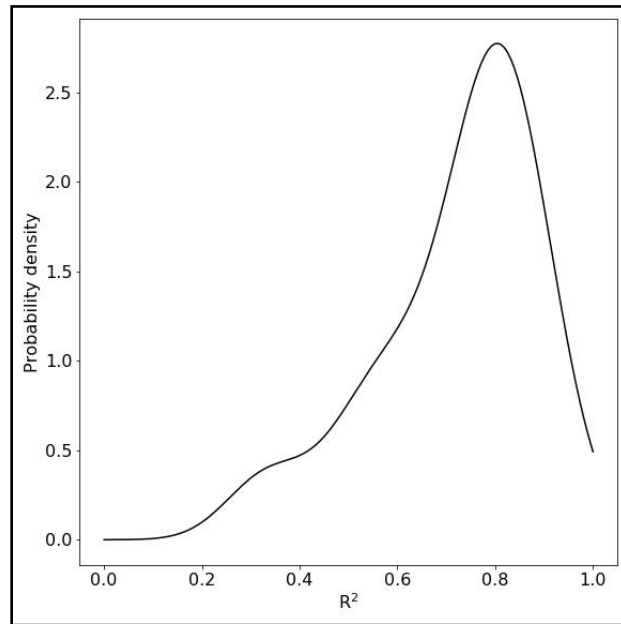


Fig. S6. Probability density of R^2 values for the relationship between the soil organic carbon index (SOCI) and soil organic carbon (SOC) for the data used to develop the logistic regression models at each of the 28 study sites.

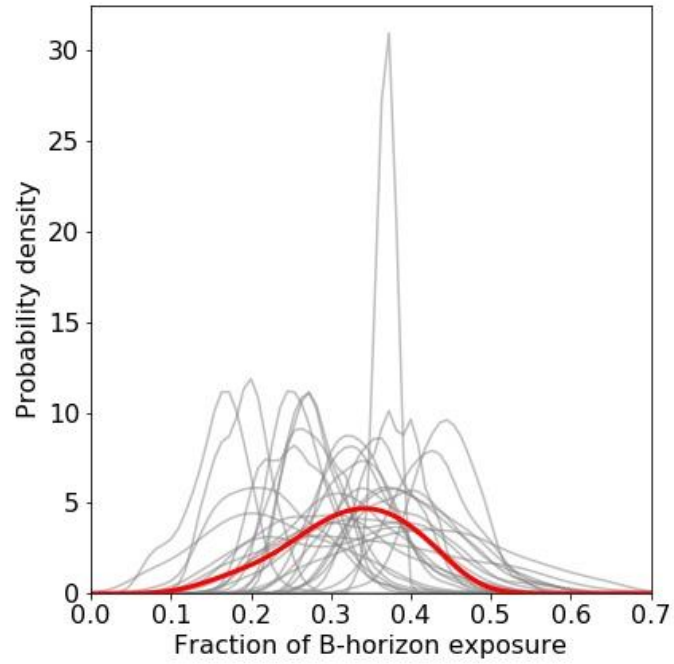


Fig. S7. Probability density of B-horizon exposure for each of the 28-sites (gray lines) generated from 500 iterations of a bootstrapped logistic regression. The red line shows the mean probability density of B-horizon exposure for all sites.

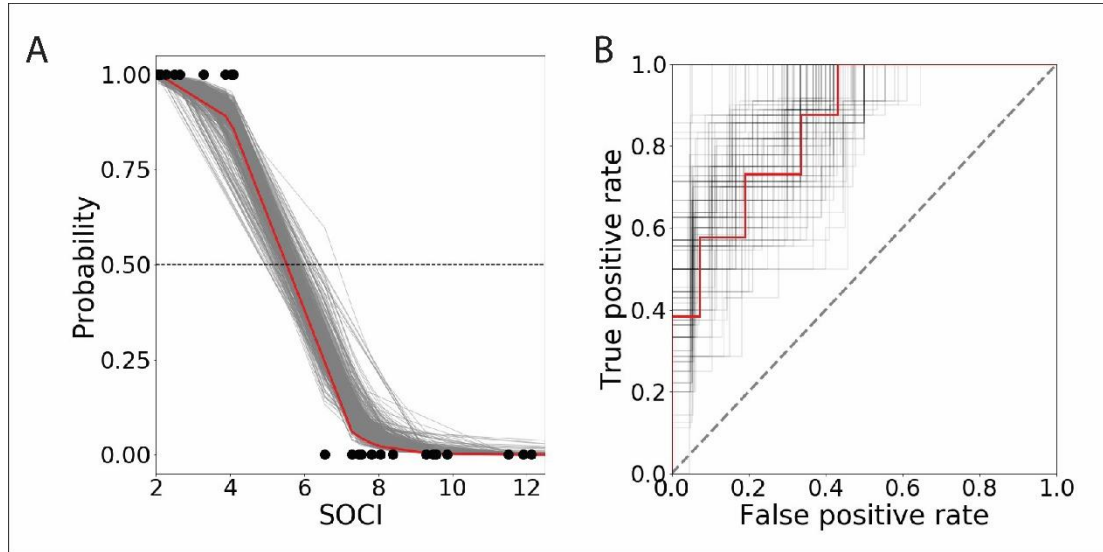


Fig. S8. Example of the logistic regression employed to classify soil horizons for the example field in Fig. 2. a) Logistic regression used for classification of A- and B-horizon soil organic carbon index (SOC) values. The SOC values for the A-horizon samples are shown at zero on the y-axis and B-horizon values are shown at 1.0. The solid red line describes the mean probability of an SOC value belonging to the B-horizon class, and the results from each of the 500 bootstrapped iterations of the logistic regression are shown in gray. The threshold SOC we use to differentiate A- and B-horizon soils is the 50% probability of an SOC value representing a B-horizon pixel. In this example, the threshold SOC is 8.0 ± 1.2 . b) The receiver operator characteristic curve for each iteration (gray lines) and the mean of all iterations (red line), which demonstrates the true- versus false positive classification rate. The mean area under the curve (AUC), which quantifies the rate of true classification, is 0.75 ± 0.06 .

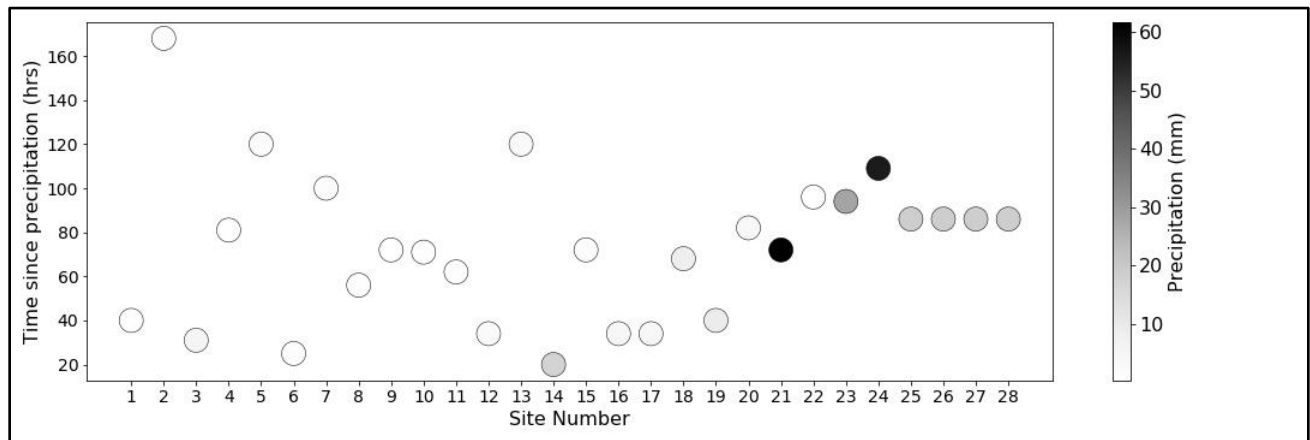


Fig. S9. Elapsed time between image acquisition and measurable precipitation and the precipitation amount for each of the 28 study sites.

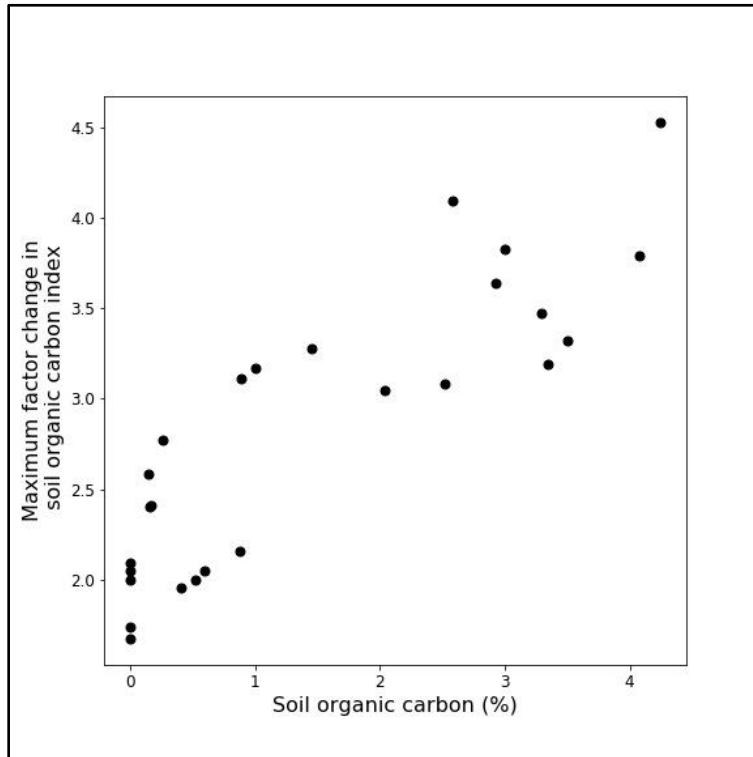


Fig. S10. The factor change in the soil organic carbon index between the dry samples and samples saturated to their maximum gravimetric moisture level for 26 soil samples as a function of soil organic carbon content.

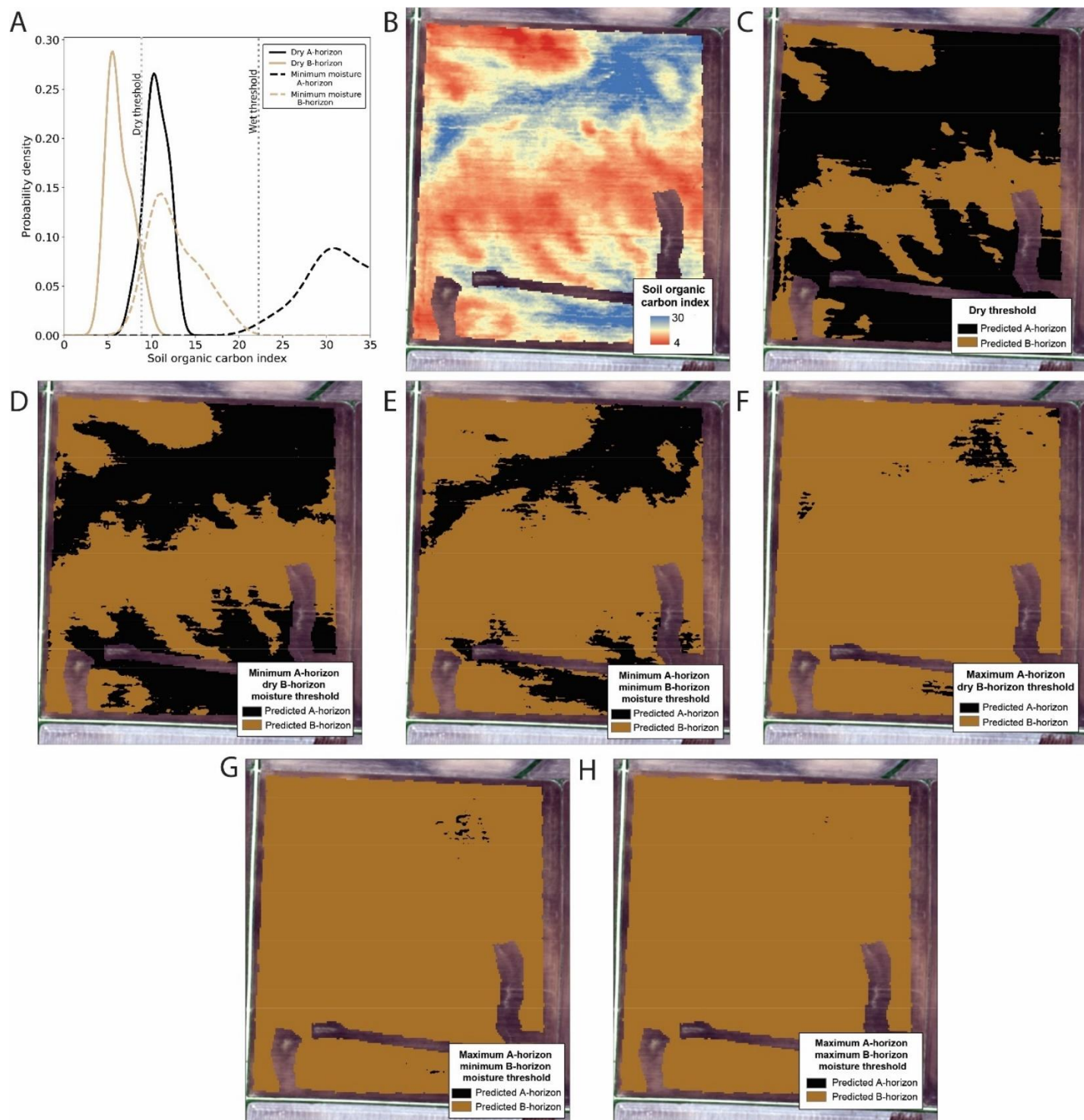


Fig. S11. An example of the threshold sensitivity to soil moisture using data from Site 2. A) Distribution of the A-horizon (black) and B-horizon (tan) soil organic carbon index (SOCi) values for the RaCA samples within 50 km of the field. The SOCi values for dry soils are shown as solid lines, and the SOCi values adjusted for soil moisture are shown as dashed lines. In this example, both the A- and B-horizon SOCi values were increased by a factor of three and two, respectively, which is the minimum response to soil moisture (from Fig. S10). Vertical dashed

lines show the SOCI value which represents the 50% probability threshold of a sample being B-horizon for the dry (light gray) and wet (dark gray) distributions. The SOCI values less than the threshold are classified as B-horizon. B) The SOCI values calculated from the satellite image, where red pixels indicate low SOCI values and blue pixels represent high SOCI values. Panels C-H demonstrate the influence of moisture-induced threshold changes on the classification of pixels. C) Pixel classification using threshold from dry samples, which is the method used in our study. D) Pixel classification using A-horizon samples shifted by the minimum moisture effect and dry B-horizon samples. E) Pixel classification using A- and B-horizon samples shifted by the minimum moisture effect. F) Pixel classification using A-horizon samples shifted by the maximum moisture effect and dry B-horizon samples. G) Pixel classification using A-horizon samples shifted by the maximum moisture effect and B-horizon samples shifted by the minimum moisture effect. H) Pixel classification using A- and B-horizon samples shifted by the maximum moisture effect. In all cases (D-H) the addition of soil moisture increases the proportion of pixels classified as B-horizon relative to the calibration based on spectra from dry soil samples (C). Image credit: ©2013 DigitalGlobe, Inc., a Maxar company, NextView License

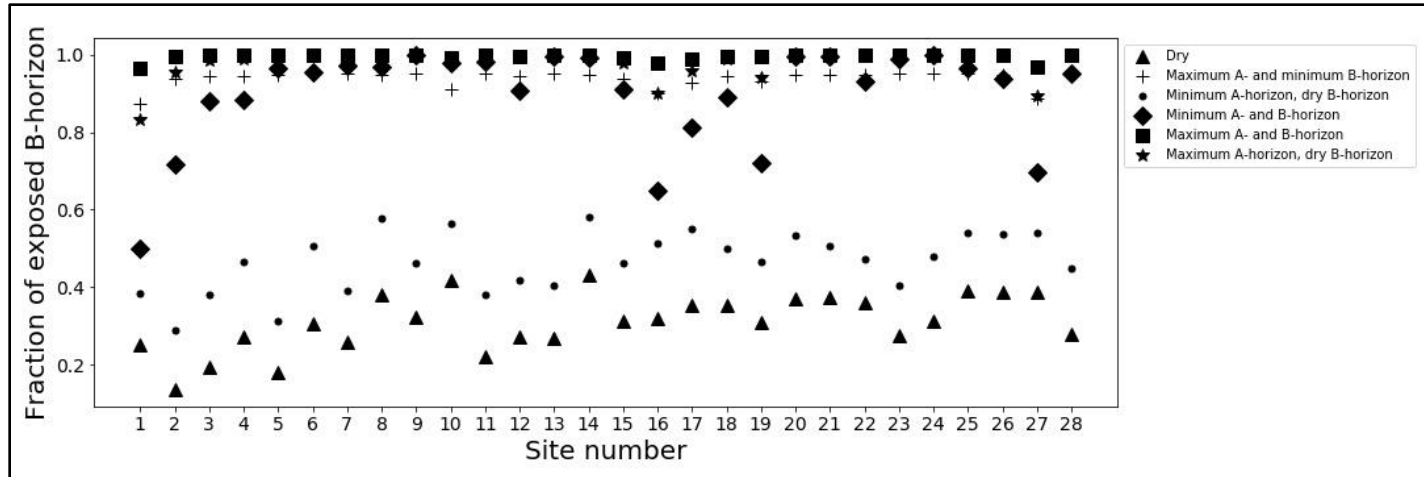


Fig. S12. The fraction of exposed B-horizon soils for each site calculated using a range of A- and B-horizon probability thresholds determined by adjusting the SOCI values measured on USDA Rapid Carbon Assessment (RaCA) soil samples to account for varying degrees of soil saturation. Triangles represent predicted B-horizon exposure using a threshold calculated from dry samples (non-adjusted values from the RaCA dataset) and are the values reported in the main text. The threshold was also calculated using soil organic carbon values adjusted for the maximum and minimum effects of soil saturation on A- and B-horizon samples (from Fig. S10). With any adjustment to the threshold to simulate moisture effects, the fraction of exposed B-horizon increases above that determined using the threshold calculated from the dry samples, indicating that our reported estimates of B-horizon exposure loss would be minimum values if the visible spectra recorded in the images we used were influenced by soil moisture.

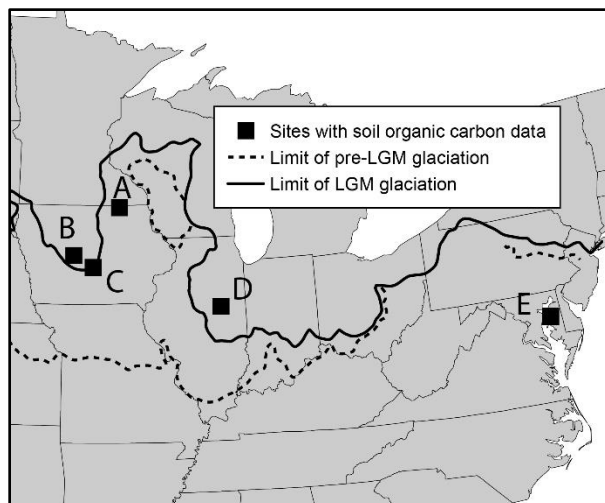


Fig. S13. Map showing locations of sites with field samples of soil organic carbon with satellite images of plowed fields with bare soil. Letters correspond to Fig. S14.

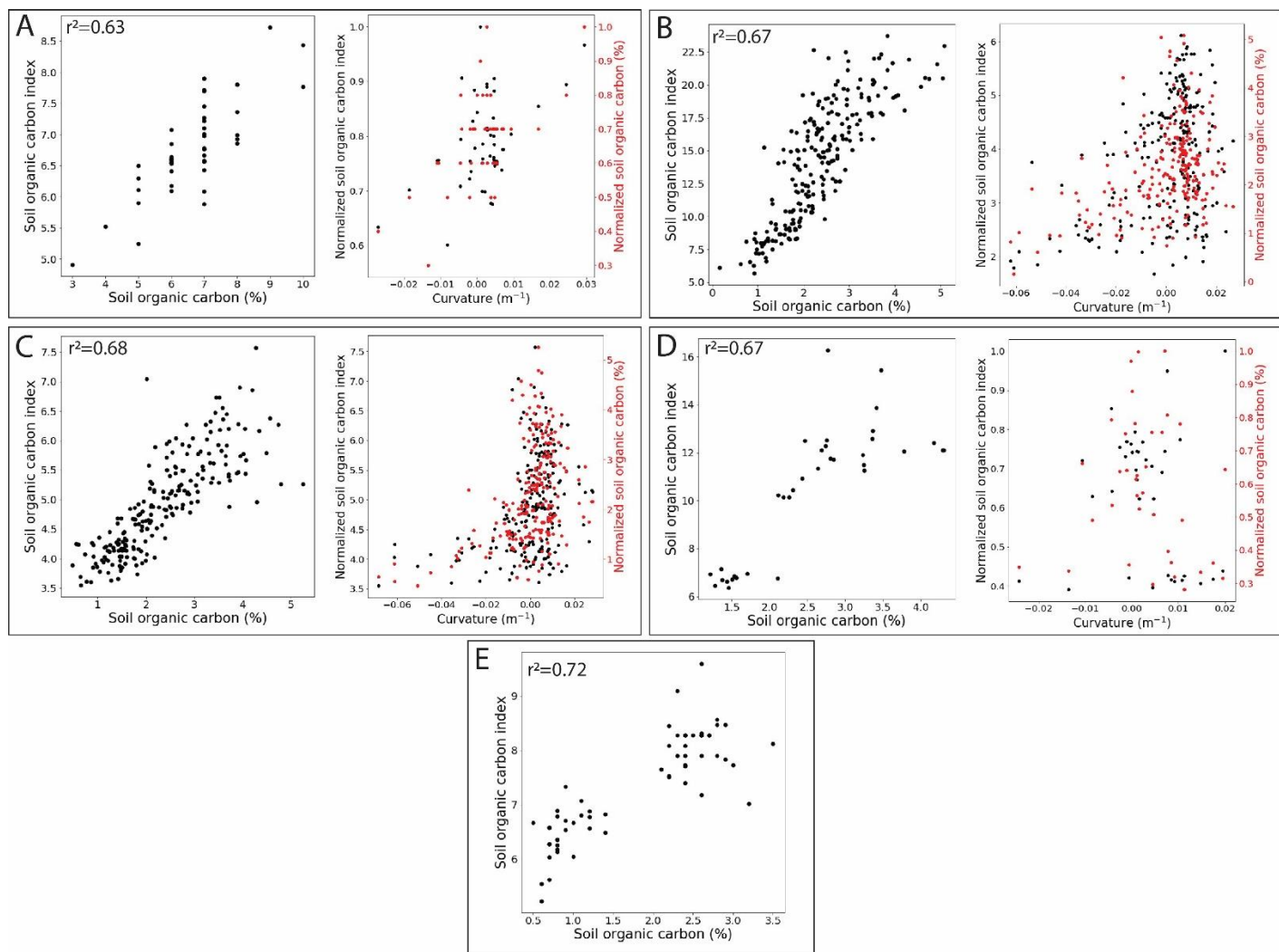


Fig. S14. The soil organic carbon index (SOCI) versus soil organic carbon (SOC) (left plot in each set) for sites A-E in Fig. S13. The normalized SOCI and normalized SOC versus topographic curvature for sites A-D (right plot in each set). The SOCI and SOC data were normalized by their maximum values to display their covariation with topographic curvature. Low soil organic carbon values are observed on convex hilltops (negative curvature), and the highest soil organic carbon values are found on concave topography (positive curvature). The R^2 values for the relationships between SOC versus curvature and the SOCI versus curvature are: Site A: 0.32 ($p < 0.01$) and 0.27 ($p < 0.01$), respectively; Site B: 0.15 ($p < 0.01$) and 0.14 ($p < 0.01$), respectively; Site C: 0.16 ($p < 0.05$) and 0.13 ($p < 0.05$), respectively; Site D: 0.1 ($p < 0.05$) and 0.1 ($p < 0.05$), respectively. Number of points for each site: A=51, B=228, C=217, D= 36, E=75.

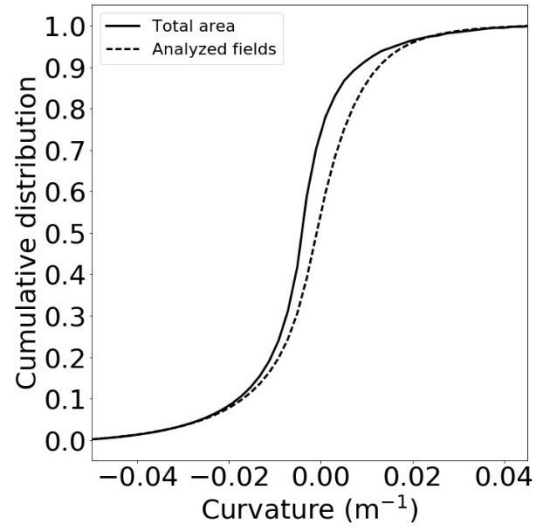


Fig. S15. Cumulative area of topographic curvature for the entire study region (solid line) and the analyzed fields (dashed line). 77% of the pixels in the full study region are located on convex topography, and 50% of pixels in the 210 km² of fields that were analyzed are on convex topography.

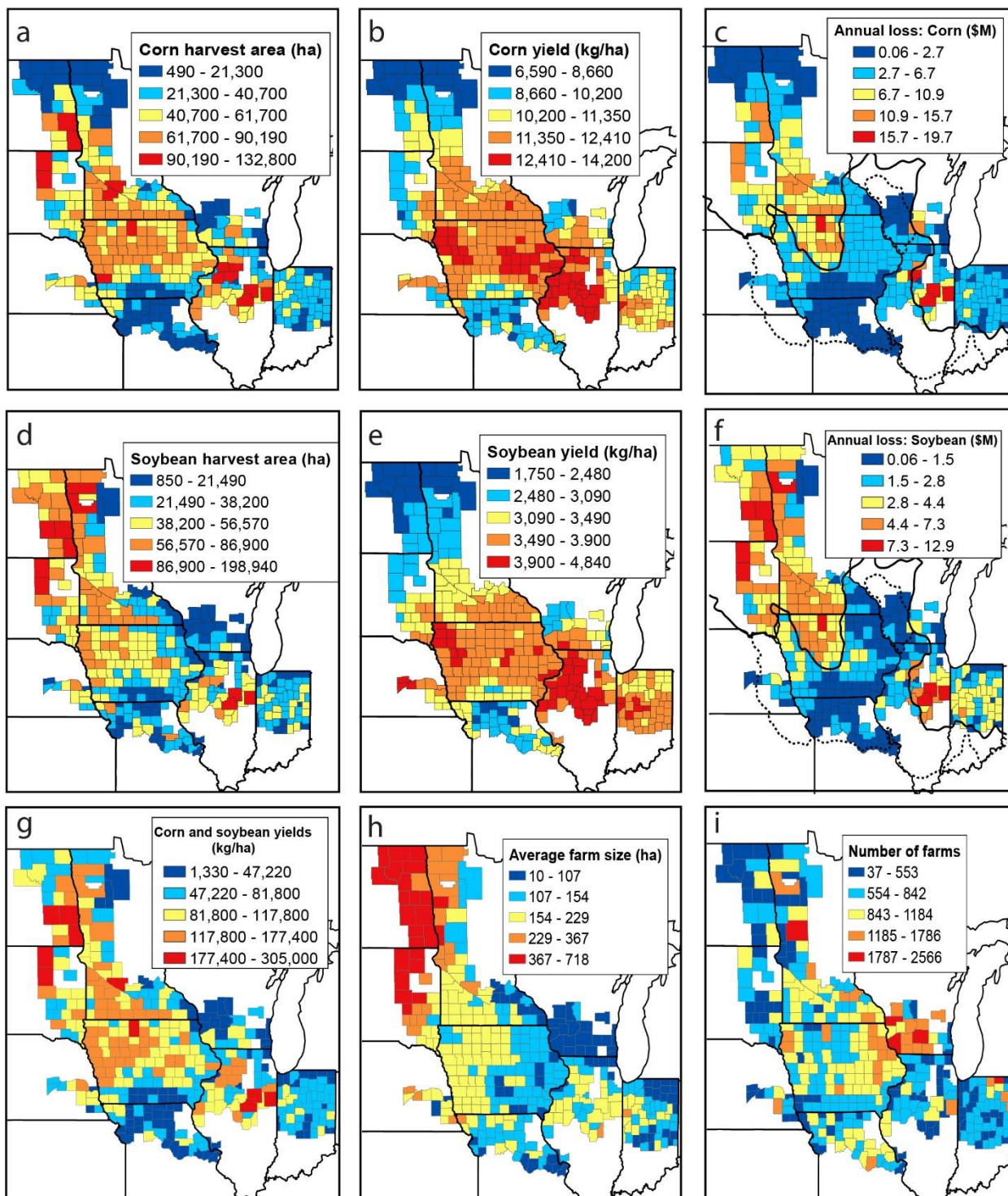
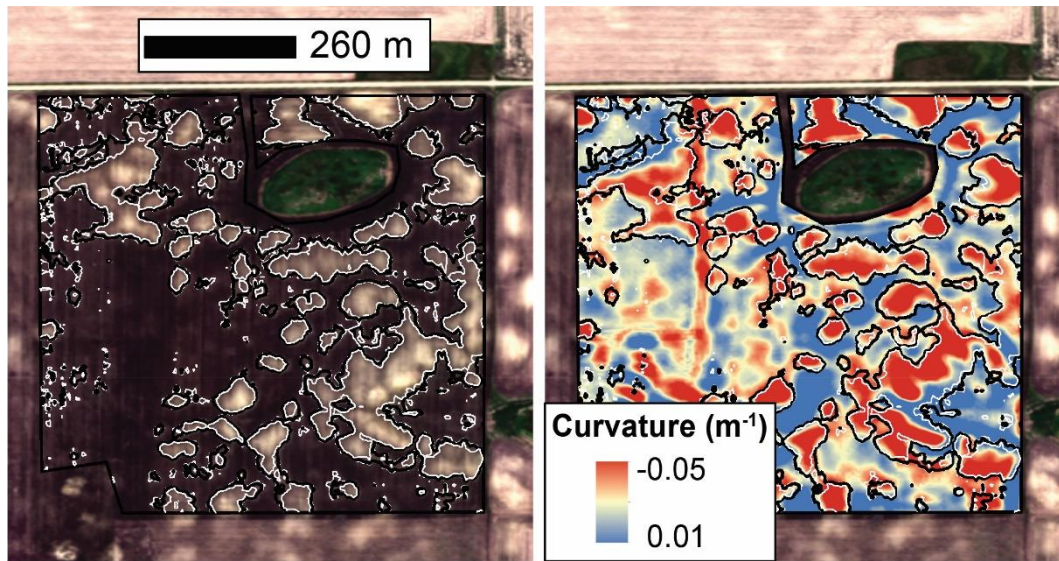
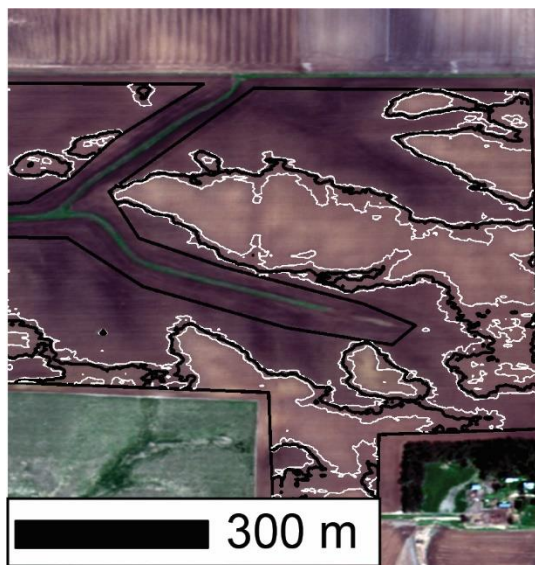


Fig. S16. Mean harvest area, mean crop yields, and mean annual economic losses for corn (a-c) and soybeans (d-f), the combined yields of corn and soybeans (g), the average farm size (h), and the number of farms in each county (i). Harvest area, yield data, number of farms are from the USDA (20). The glacial extent prior to the LGM and the extent during the LGM are shown as dashed and solid lines, respectively.

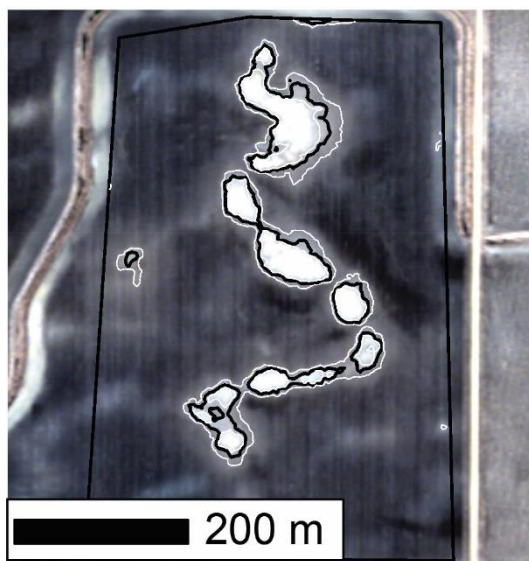
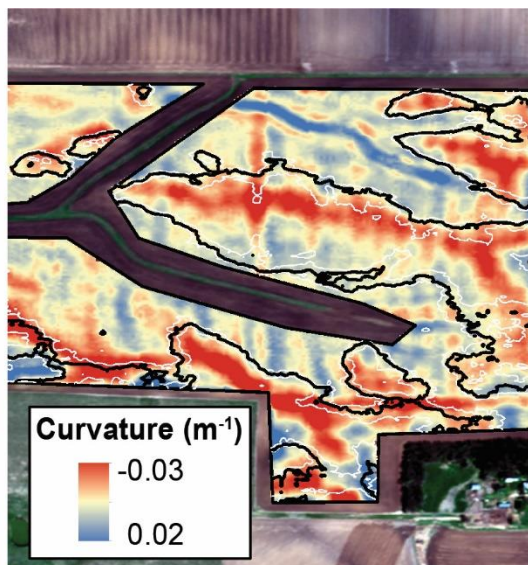
Fig. S17. [Below] Examples of B-horizon exposure and topographic curvature from each of our 28 study sites. The left panel is a true-color image with black polygons surrounding light-colored areas predicted to have exposed B-horizon soil, and white polygons indicate ± 1 S.D. of the predicted area of B-horizon exposure. The right panel is a topographic curvature map where red pixels denote negative curvature (convex topography) and blue pixels denote positive curvature (concave topography). The exposure of B-horizon soils is readily observable within each field, as is the spatial correlation between B-horizon exposure and negative curvature, which demonstrates the validity of our method. Image credit: ©2013-2016 DigitalGlobe, Inc., a Maxar company, NextView License.



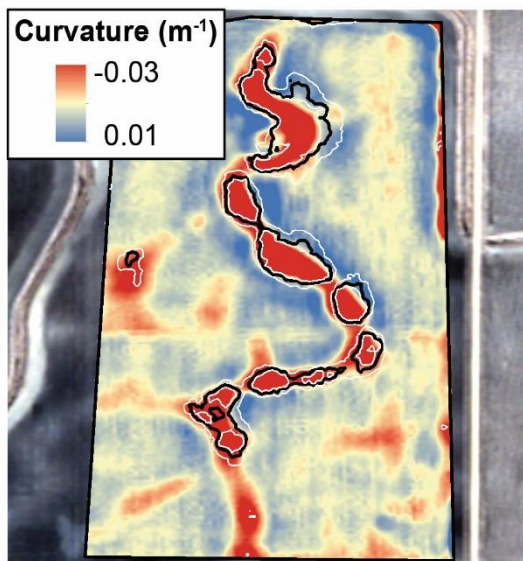
Site 1

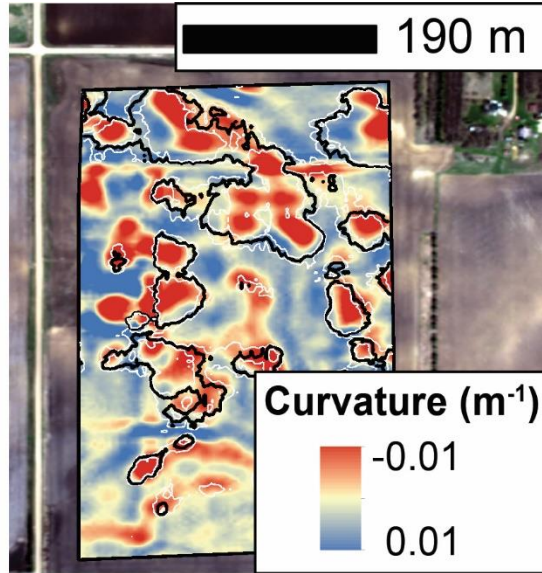
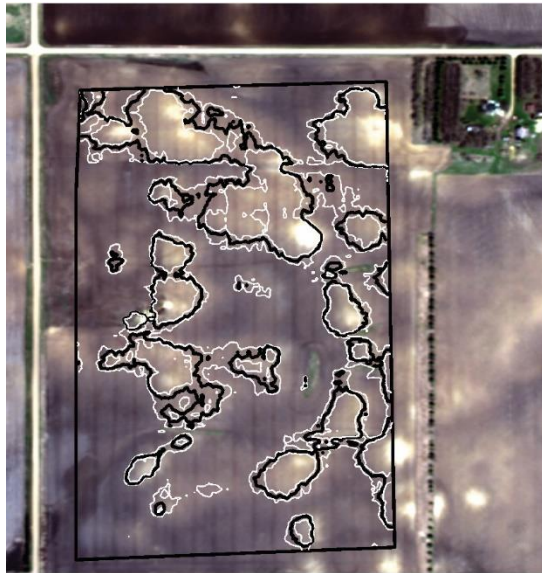


Site 2

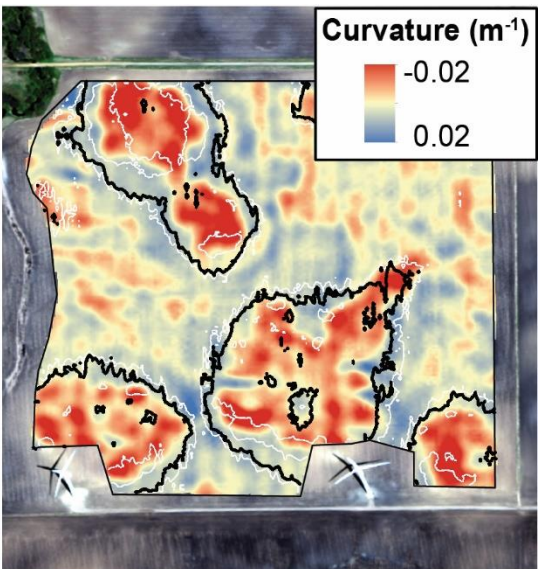
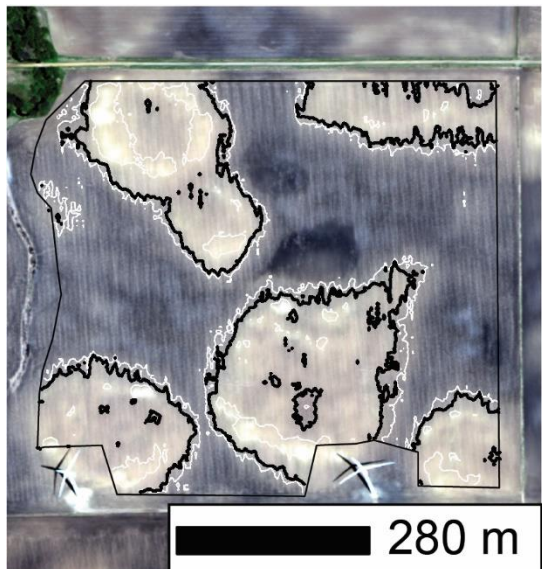


Site 3

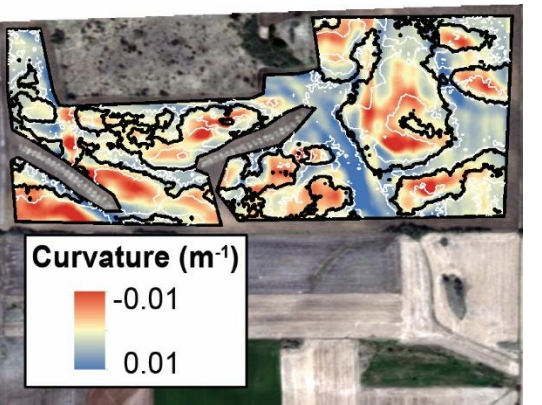




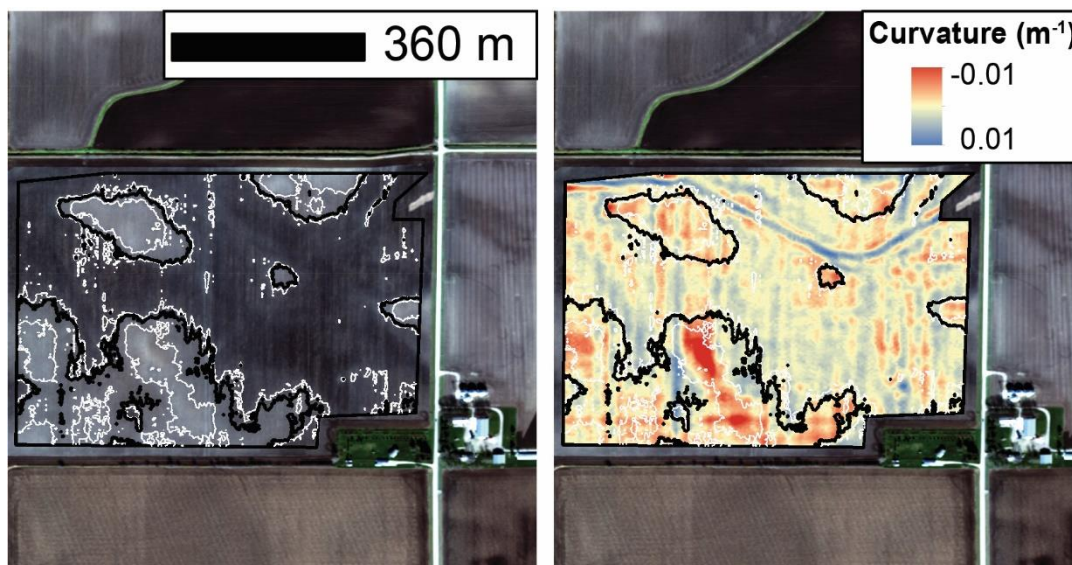
Site4



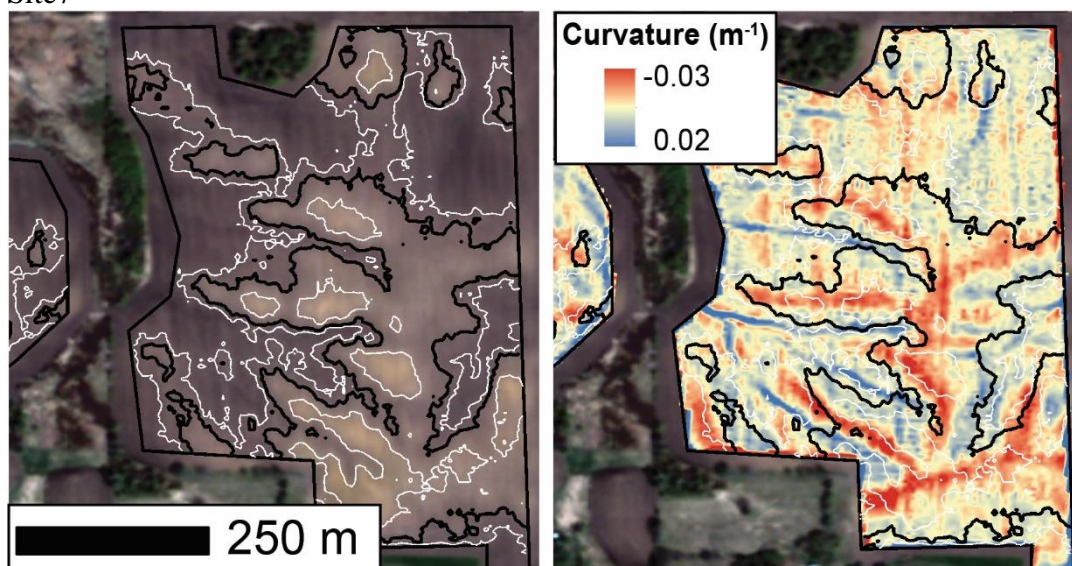
Site5



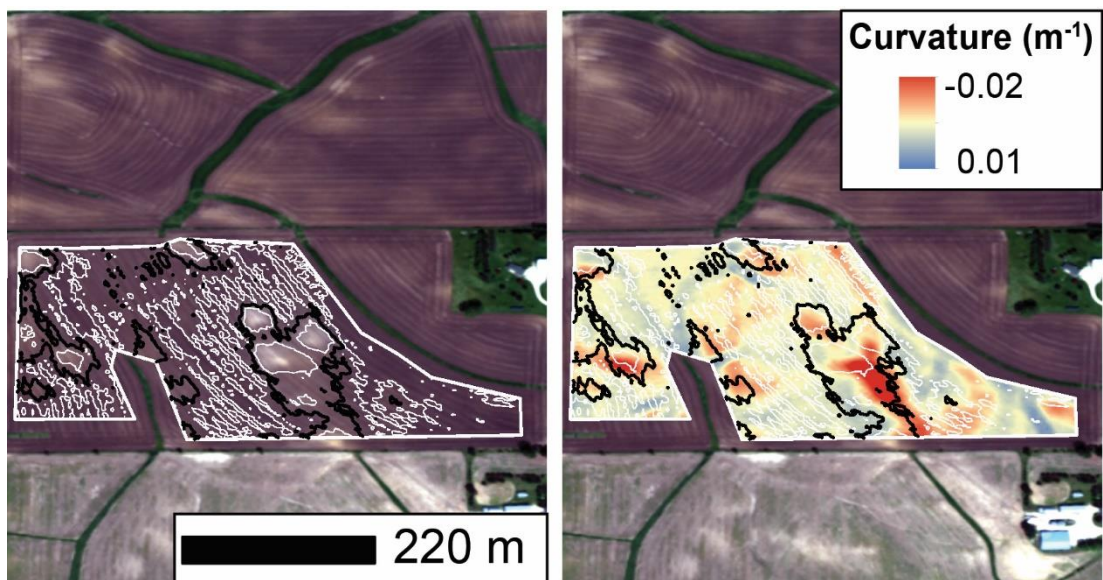
Site6



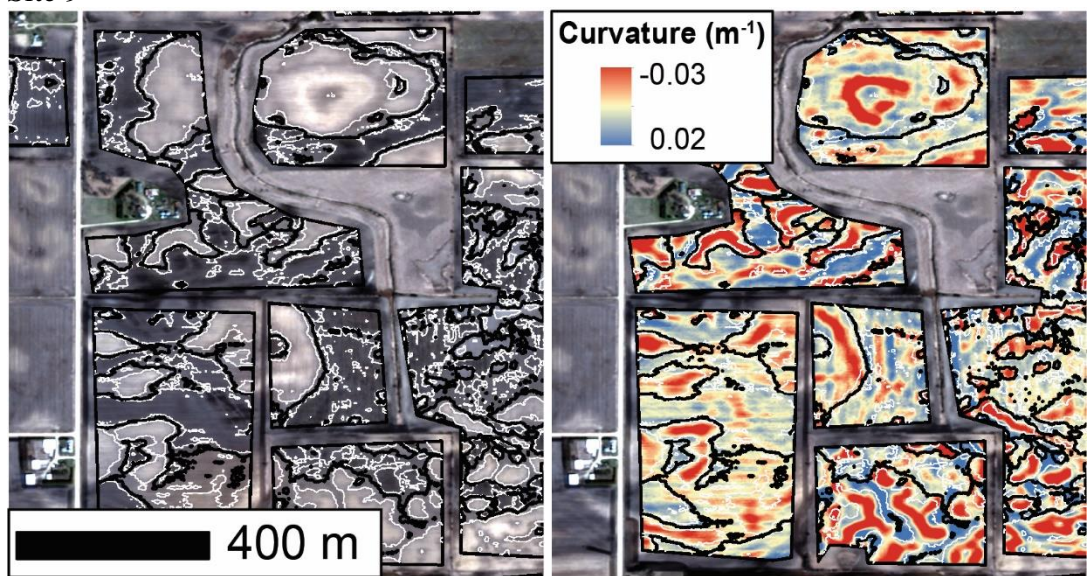
Site7



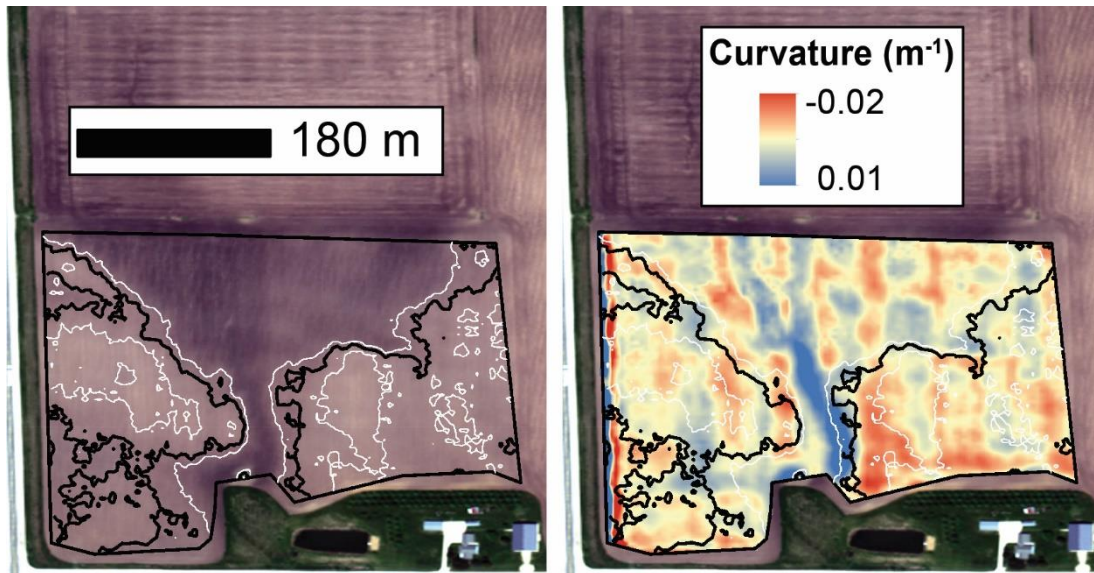
Site8



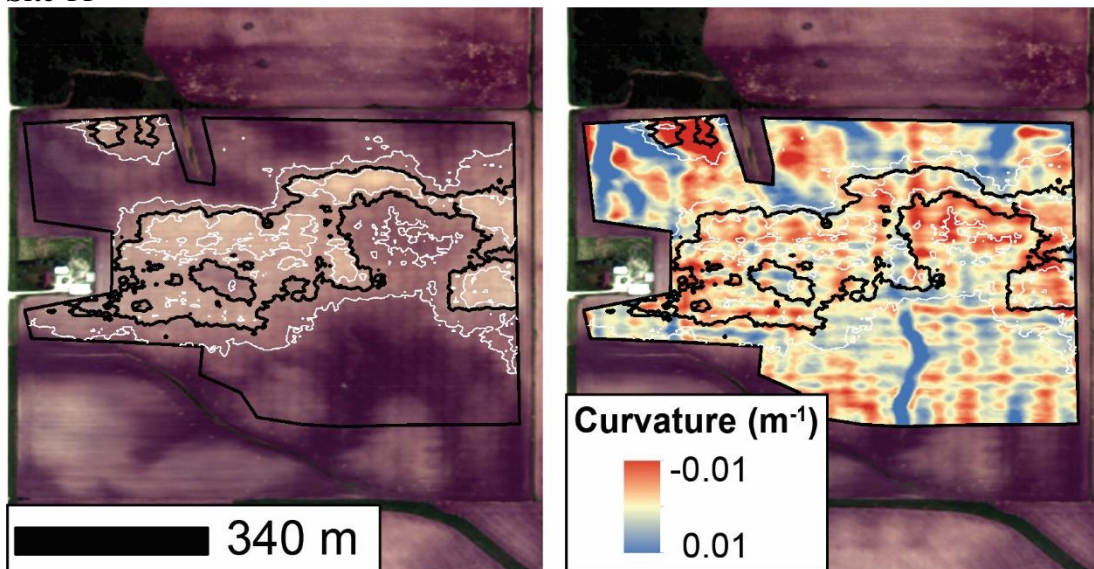
Site 9



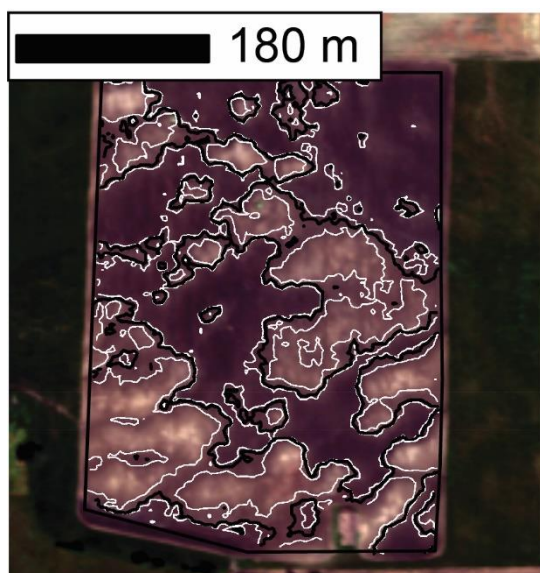
Site 10



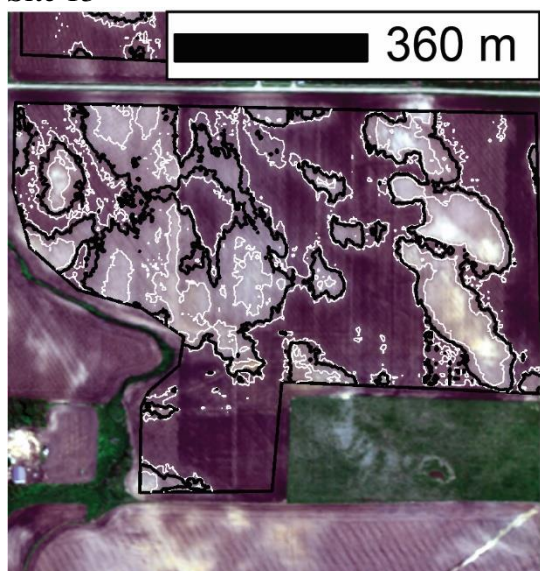
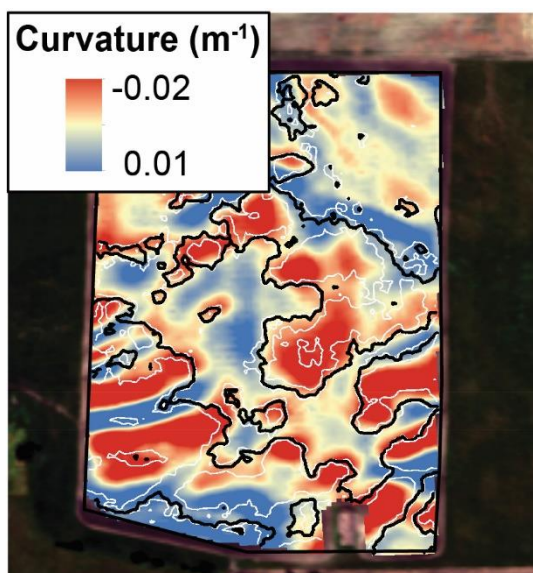
Site 11



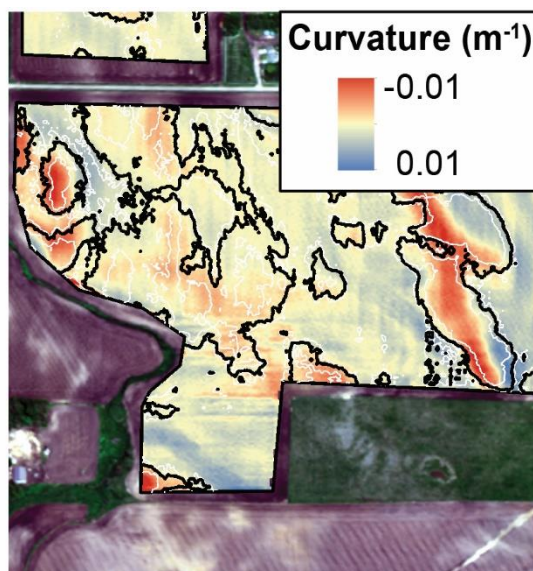
Site 12

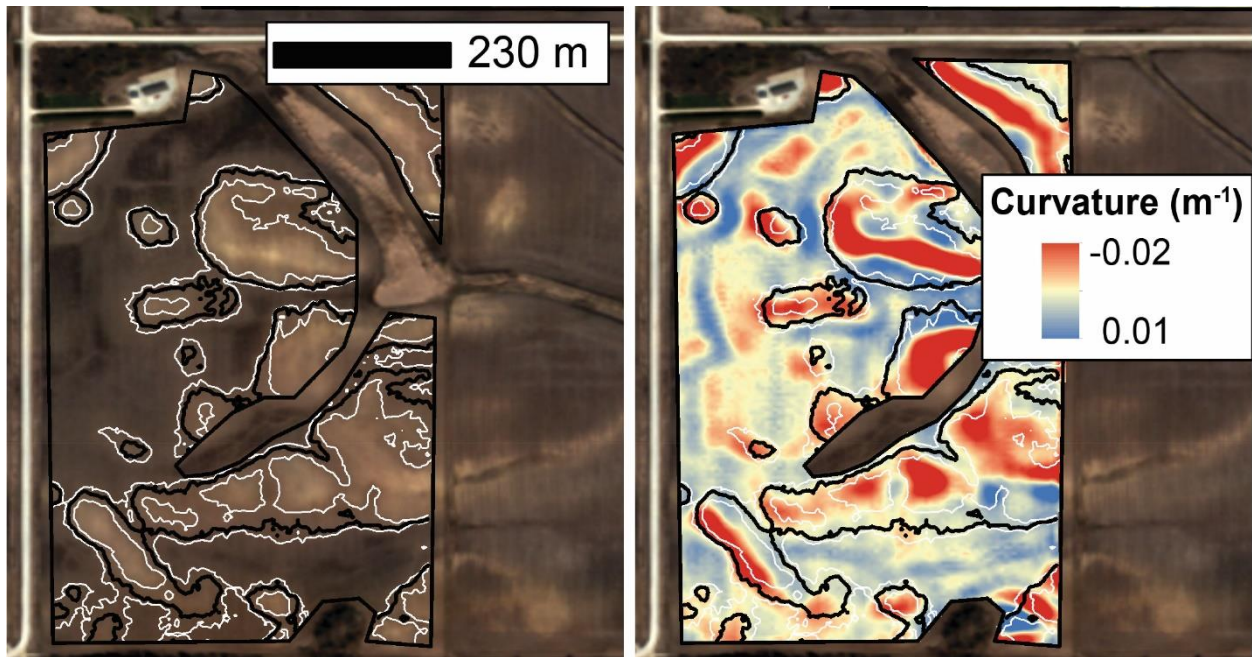


Site 13

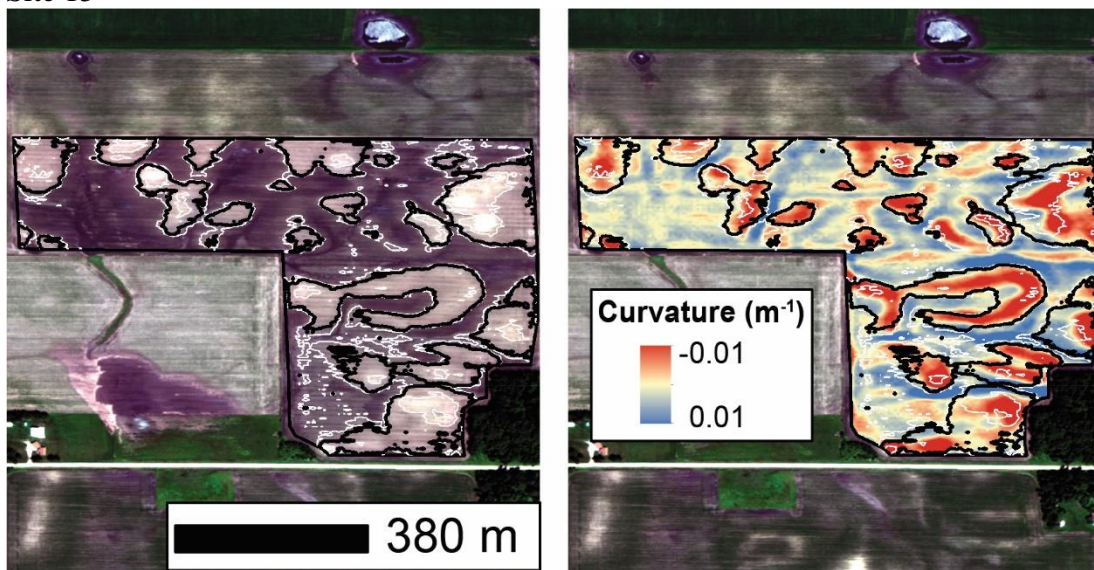


Site 14

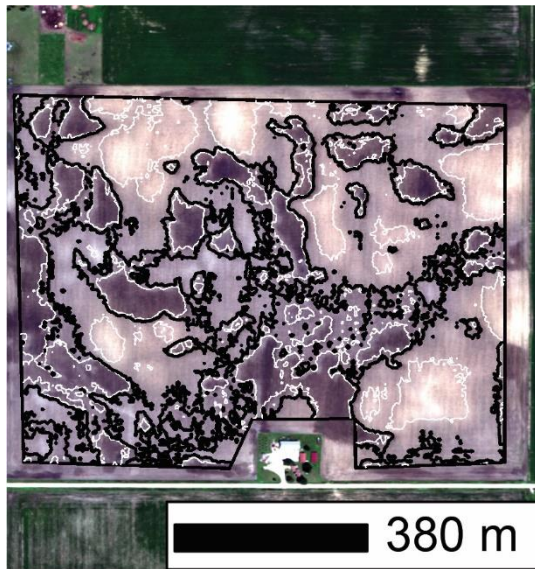




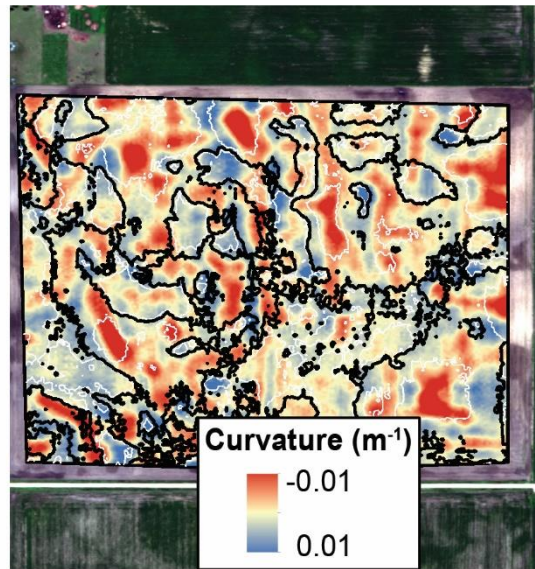
Site 15



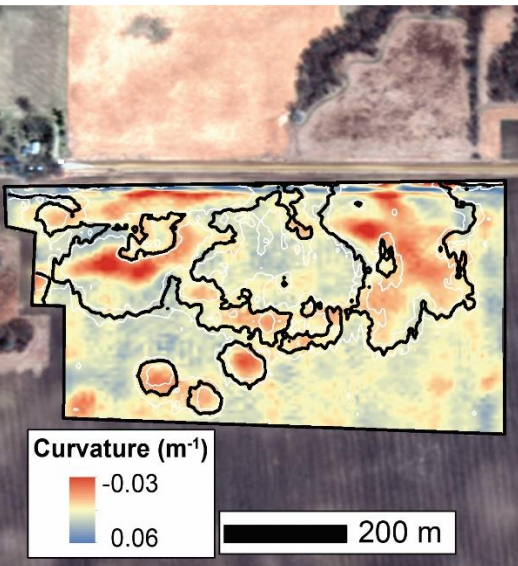
Site 16

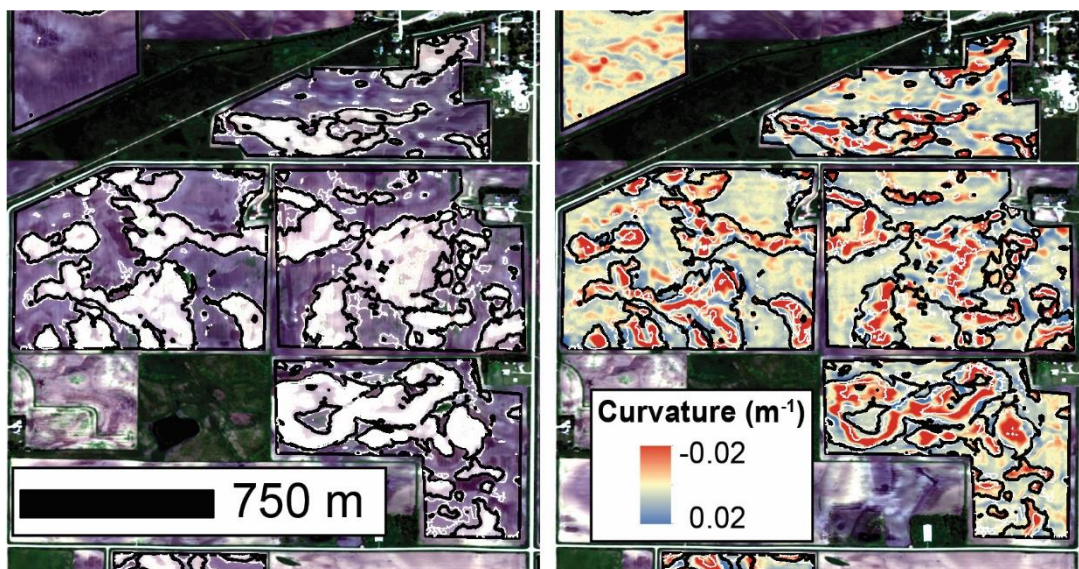


Site 17

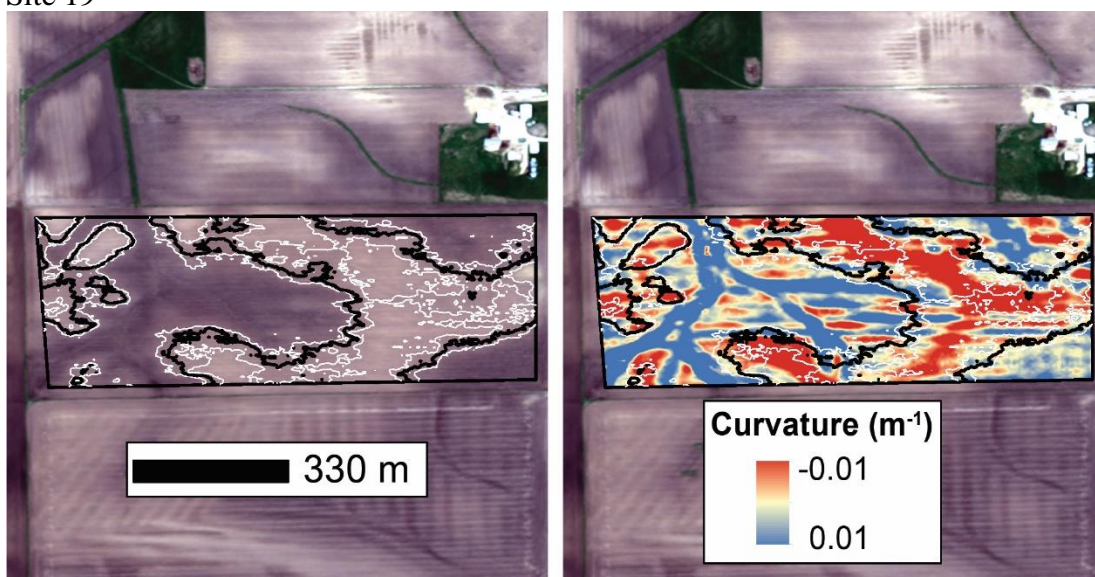


Site 18

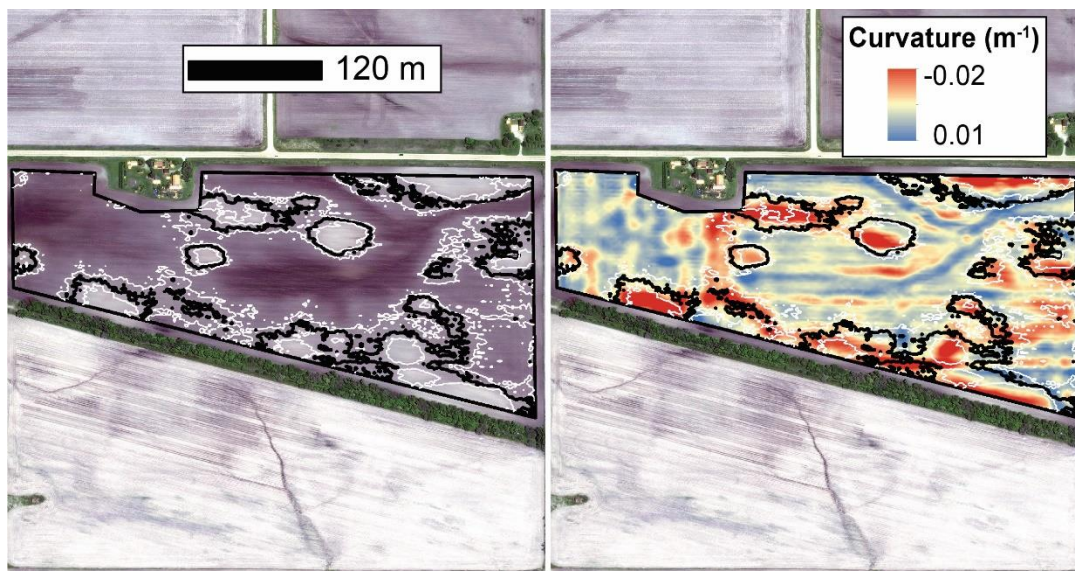




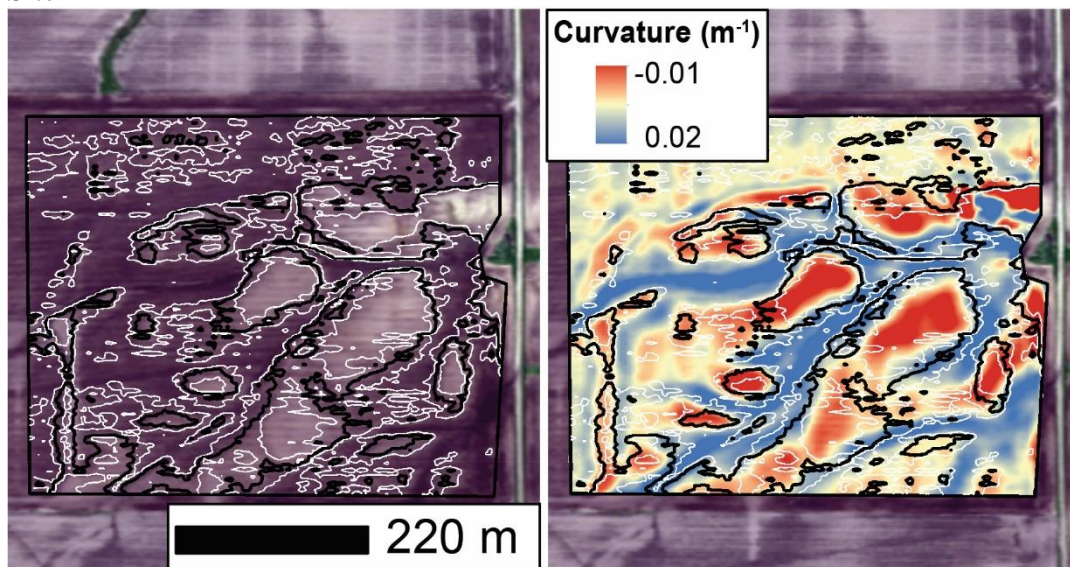
Site 19



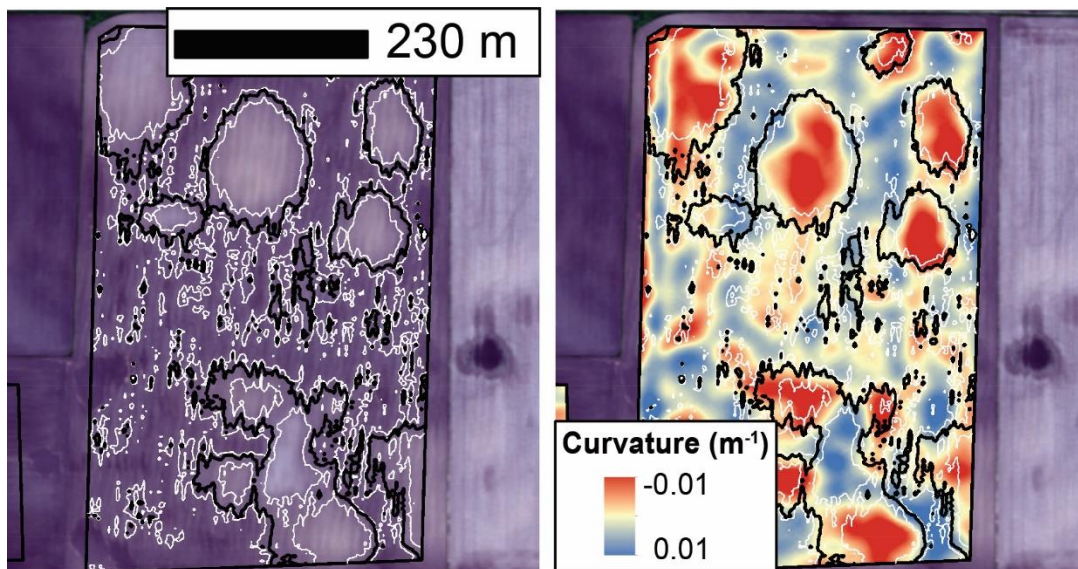
Site 20



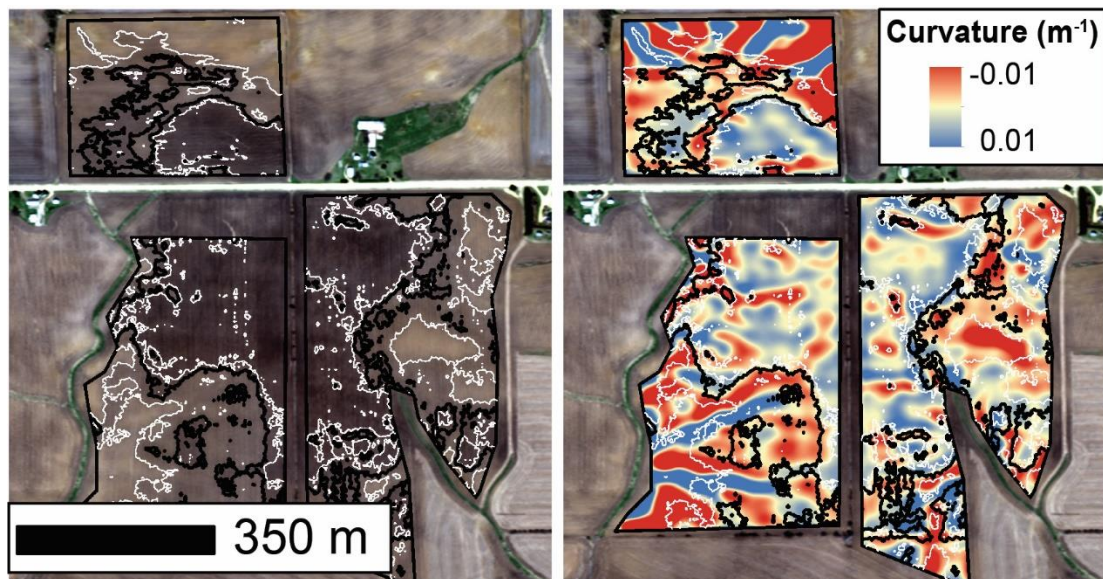
Site 21



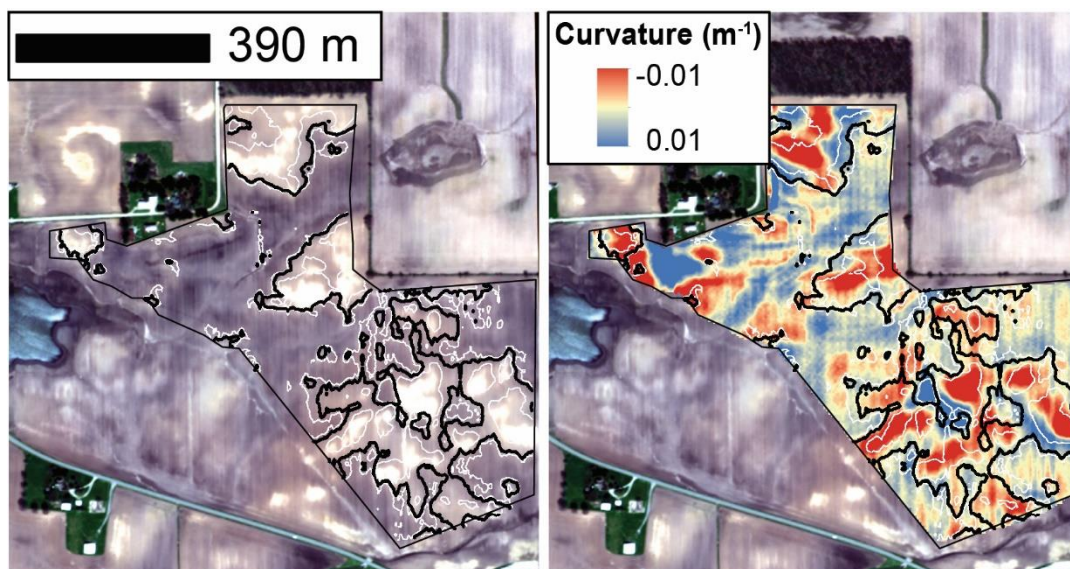
Site 22



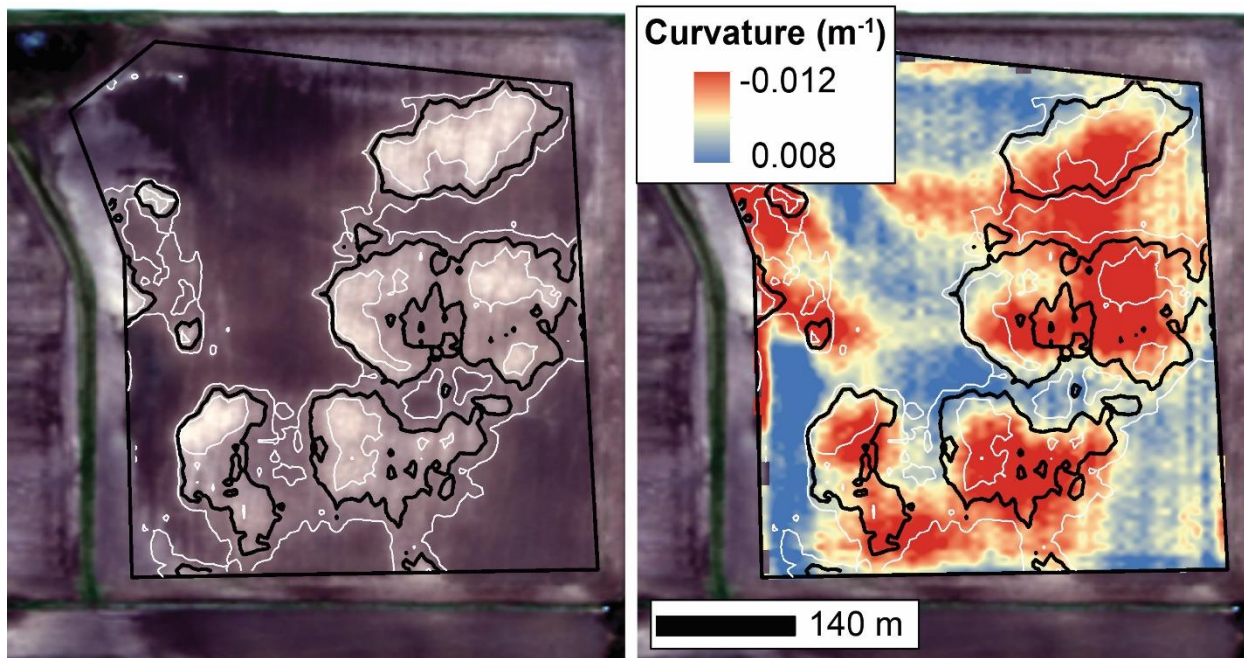
Site 23



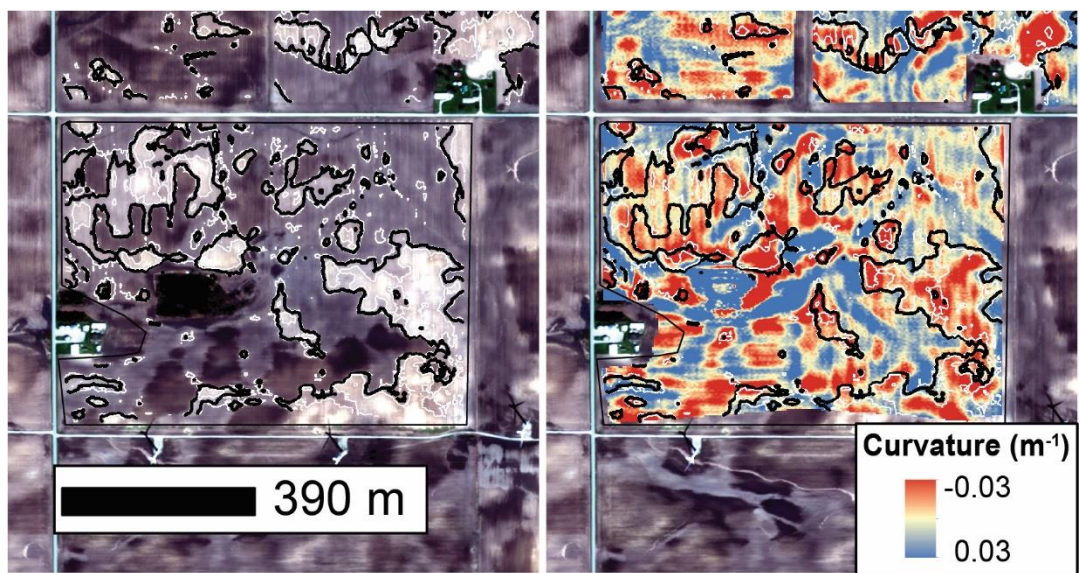
Site 24



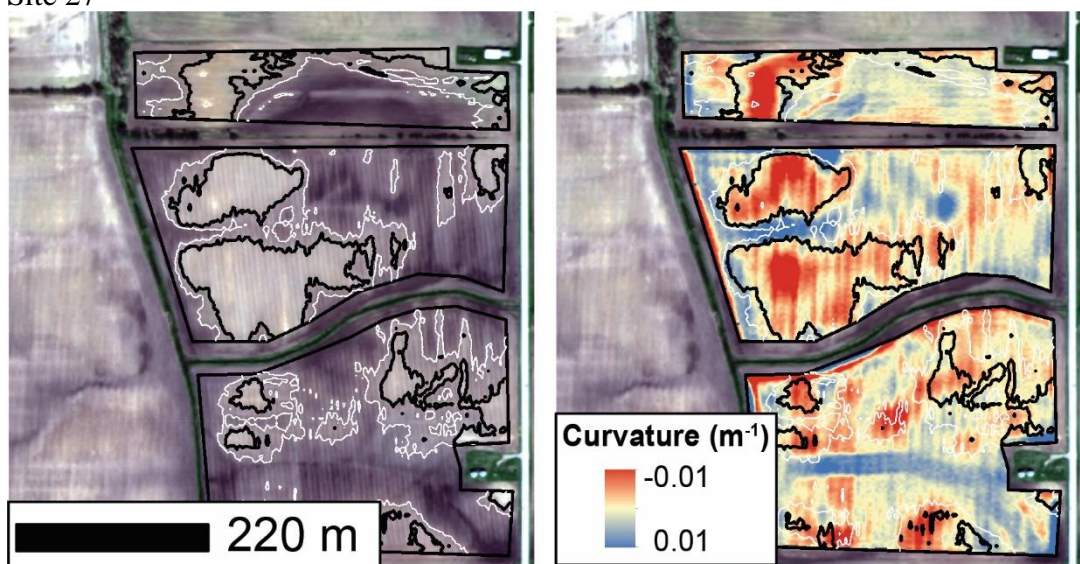
Site 25



Site 26



Site 27



Site 28

Table S1. Citations, locations, and A-horizon thicknesses for 28 samples collected in native tallgrass prairies. The mean A-horizon thickness is 37 cm.

Study	Location	A-horizon thickness (cm)
Weaver and Hanson, 1941 (27)	Nebraska	45
Bockheim and Hartemink, 2017 (28)	Wisconsin	36
		25
		51
		23
Blank and Fosberg, 1989 (29)	South Dakota	25

Steiger, 1930 (30)	Nebraska	43
Hirmas et al., 2013 (31)	Kansas	16
Rusle and Engle, 1925 (32)	Nebraska	30
Wills, 2005 (33)	Iowa	43
		30
		35
		48
		55
		24
		46
		48
		26
		42
		39
		47
		41
		44
		35
		39
		32
		36
		40
		40
		38

References

1. Manies KL, Harden JW, Kramer L & Parton WJ (2001) Carbon dynamics within agricultural and native sites in the loess region of western Iowa. *Global Change Biol* 7: 545-555.
2. Thaler EA, Larsen IJ & Yu Q (2019) A new index for remote sensing of soil organic carbon based solely on visible wavelengths. *Soil Sci Soc Am J* 83: 1443-1450.
3. Mishra U, *et al* (2009) Predicting soil organic carbon stock using profile depth distribution functions and ordinary kriging. *Soil Sci Soc Am J* 73: 614-621.
4. U.S. Geological Survey, 2019, The National Map—New data delivery homepage, advanced viewer, lidar visualization: US. Geological Survey Fact Sheet.
5. Roering JJ, Marshall J, Booth AM, Mort M & Jin Q (2010) Evidence for biotic controls on topography and soil production. *Earth Planet Sci Lett* 298: 183-190.

6. Neigh CS, Masek JG & Nickeson JE (2013) High-resolution satellite data open for government research. *Eos, Transactions American Geophysical Union* 94: 121-123.
7. Smith GM & Milton EJ (1999) The use of the empirical line method to calibrate remotely sensed data to reflectance. *Int J Remote Sens* 20: 2653-2662.
8. Baldridge AM, Hook SJ, Grove CI & Rivera G (2009) The ASTER spectral library version 2.0. *Remote Sens Environ* 113: 711-715.
9. Willis, S., Loecke, T., Sequeira, C., Teachman, G., Grunwald, S., and West, L.T., 2014. Overview of the US rapid carbon assessment project: sampling design, initial summary and uncertainty estimates. In Soil Carbon, A.E. Hartemink, K. McSweeney (Eds.), Springer International Publishing, Cham. 95-104.
10. Sequeira CH, *et al* (2014) Development and update process of VNIR-based models built to predict soil organic carbon. *Soil Sci Soc Am J* 78: 903-913.
11. Wijewardane NK, Ge Y, Wills S & Loecke T (2016) Prediction of soil carbon in the conterminous united states: Visible and near infrared reflectance spectroscopy analysis of the rapid carbon assessment project. *Soil Sci Soc Am J* 80: 973-982.
12. Capehart WJ & Carlson TN (1997) Decoupling of surface and near-surface soil water content: A remote sensing perspective. *Water Resour Res* 33: 1383-1395.
13. Nocita M, Stevens A, Noon C & van Wesemael B (2013) Prediction of soil organic carbon for different levels of soil moisture using vis-NIR spectroscopy. *Geoderma* 199: 37-42.
14. Wilson CG, *et al* (2018) The intensively managed landscape critical zone observatory: A scientific testbed for understanding critical zone processes in agroecosystems. *Vadose Zone Journal* 17(1)
15. Wills SA, Burras CL & Sandor JA (2007) Prediction of soil organic carbon content using field and laboratory measurements of soil color. *Soil Sci Soc Am J* 71: 380-388.
16. Li X, McCarty GW, Karlen DL & Cambardella CA (2018) Topographic metric predictions of soil redistribution and organic carbon in Iowa cropland fields. *Catena* 160: 222-232.
17. Hively WD, *et al* (2011) Use of airborne hyperspectral imagery to map soil properties in tilled agricultural fields. *Applied and Environmental Soil Science*. 2011:1-13.
18. Fullerton DS, Bush CA & Pennell JN (2004) Map of surficial deposits and materials in the eastern and central united states (east of 102 west longitude). *US Geological Survey Geologic Investigation Series I-2789*

19. Leigh DS & Knox JC (1994) Loess of the upper Mississippi Valley Driftless Area. *Quatern Res* 42: 30-40.
20. United States Department of Agriculture, National Agricultural Statistics Service (2017) Quick Stats 2.0. <https://quickstats.nass.usda.gov>. Accessed 11/27/2019
21. Fenton TE (2012) The impact of erosion on the classification of mollisols in iowa. *Can J Soil Sci* 92(3): 413-418.
22. USDA Economic Research Service (2017) Farm income and wealth statistics. economic research service, department of agriculture. <https://Data.nal.usda.gov/dataset/farm-income-and-wealth-statistics>
23. U.S. Department of Agriculture (2018) Farms and land in farms 2017 Summary ISSN: 1995-726 2004. https://www.nass.usda.gov/Publications/Todays_Reports/reports/fnlo0419.pdf.
24. Thaler, EA., IJ. Larsen, Q. Yu. (2020) Remote sensing derived topsoil and agricultural economic losses, midwestern USA. *ORNL DAAC, Oak Ridge, Tennessee, USA*.
25. Soil Science Division Staff (2017) Soil survey manual. *USDA Handbook 18*: 120-131.
26. Sanderman J, Hengl T & Fiske GJ (2017) Soil carbon debt of 12,000 years of human land use. *Proc Natl Acad Sci U S A* 114: 9575-9580.
27. Weaver JE & Hansen WW (1941) Regeneration of native midwestern pastures under protection
28. Bockheim JG & Hartemink AE (2017) *The soils of Wisconsin*. World soils book series. Springer, Cham, Switzerland.
29. Blank RR & Fosberg MA (1989) Cultivated and adjacent virgin soils in northcentral South Dakota I. chemical and physical comparisons. *Soil Sci Soc Am J* 53: 1484-1490.
30. Steiger TL (1930) Structure of prairie vegetation. *Ecology* 11: 170-217.
31. Hirmas DR, Giménez D, Subroy V & Platt BF (2013) Fractal distribution of mass from the millimeter-to decimeter-scale in two soils under native and restored tallgrass prairie. *Geoderma* 207: 121-130.
32. Russell JC & Engle LG (1925) Soil horizons in the central prairies. *Soil Sci Soc Am J* 6: 1-18.
33. Wills SA (2005) The spatial distribution of soil properties and prediction of soil organic carbon in Hayden prairie and an adjacent agricultural field. <https://doi.org/10.31274/rtd-180813-11585>